



Epigenetic cell fate in *Candida albicans* is controlled by transcription factor condensates acting at super-enhancer-like elements

Corey Frazer^{1,7}, Mae I. Staples^{1,7}, Yoori Kim², Matthew Hirakawa¹, Maureen A. Dowell¹, Nicole V. Johnson², Aaron D. Hernday³, Veronica H. Ryan¹⁴, Nicolas L. Fawzi¹⁵, Ilya J. Finkelstein¹⁶ and Richard J. Bennett¹[✉]

Cell identity in eukaryotes is controlled by transcriptional regulatory networks that define cell-type-specific gene expression. In the opportunistic fungal pathogen *Candida albicans*, transcriptional regulatory networks regulate epigenetic switching between two alternative cell states, 'white' and 'opaque', that exhibit distinct host interactions. In the present study, we reveal that the transcription factors (TFs) regulating cell identity contain prion-like domains (PrLDs) that enable liquid–liquid demixing and the formation of phase-separated condensates. Multiple white–opaque TFs can co-assemble into complex condensates as observed on single DNA molecules. Moreover, heterotypic interactions between PrLDs support the assembly of multifactorial condensates at a synthetic locus within live eukaryotic cells. Mutation of the *Wor1* TF revealed that substitution of acidic residues in the PrLD blocked its ability to phase separate and co-recruit other TFs in live cells, as well as its function in *C. albicans* cell fate determination. Together, these studies reveal that PrLDs support the assembly of TF complexes that control fungal cell identity and highlight parallels with the 'super-enhancers' that regulate mammalian cell fate.

Many species can epigenetically differentiate into alternative cellular subtypes. This ability relies on transcriptional regulatory networks (TRNs) to coordinate cell type-specific gene expression programmes that are then maintained over multiple cell divisions^{1,2}. In mammalian cells, studies suggest that cell fate is determined by transcription factors (TFs) undergoing liquid–liquid phase separation (LLPS), whereby protein-dense condensates form that are in equilibrium with a more dilute surrounding phase^{3–10}. The high densities of TFs required for LLPS are achieved by recruitment to unusually large regulatory regions or 'super-enhancers' that control cell type identity^{11–14}. Super-enhancers consist of clusters of conventional enhancers that are in close proximity to each other, which can account for the high density of TFs bound to these regions as well as for their extended size^{9,11,14–18}.

Although cell fate determination has been extensively studied in multicellular organisms, many unicellular pathogens also undergo differentiation to evade the immune system or to adapt to fluctuating host environments^{19–22}. A prime example of epigenetic variation is phenotypic switching in the fungal pathogen *Candida albicans*, where cells interconvert between white and opaque states that display distinct phenotypic properties and tissue tropisms^{20,23–26}. Regulation of the white–opaque switch involves a complex network of at least eight TFs which autoregulate their own expression as well as that of each other^{27–36}. In the present study, we reveal that seven of these master TFs contain prion-like domains (PrLDs) that promote co-assembly into phase-separated condensates. These PrLDs enable homotypic and heterotypic interactions between TFs *in vivo* and are critical for TF function in cell fate determination. We therefore

propose that LLPS allows coordination of TFs for regulation of fungal cell fate and reveal parallels to the cell fate-defining networks controlling mammalian cell identity.

Results

The TF network regulating *C. albicans* white–opaque cell identity. *C. albicans* cells can stochastically switch between white and opaque states that have distinct morphologies and transcriptional programmes. At the colony level, switching is evident from darker opaque sectors within white colonies and can be readily detected by state-specific fluorescent reporters (Fig. 1a,b)^{37–39}. The TRN regulating the white–opaque switch shows multiple parallels to those defining mammalian cell fate. In both, cell identity is controlled by interconnected networks whereby TFs autoregulate their own expression as well as that of each other. For example, in the white–opaque network, connections exist between eight master TFs (Fig. 1c)^{27–36}. The TRNs regulating cell identity also involve unusually large regulatory regions in both fungi and mammals. The median size of mammalian 'super-enhancers' is >8 kb versus ~700 bp for typical enhancers¹¹, and the regulatory regions of master white–opaque TFs are similarly expanded; the upstream intergenic regions of 6 of the 8 TFs are >7 kb, considerably larger than the average intergenic length of 557 bp in *C. albicans*⁴⁰. White–opaque TFs bind overlapping regions upstream of the genes encoding the master TFs. For example, the intergenic region upstream of *WOR1* is 10.5 kb and is bound by all eight master TFs in opaque cells, including *Wor1* itself (Fig. 1d)^{27,30,36}. Similar patterns of TF binding are observed for intergenic regions upstream of the other master TFs in the TRN

¹Department of Molecular Microbiology and Immunology, Brown University, Providence, RI, USA. ²Department of Molecular Biosciences and Institute for Cellular and Molecular Biology, University of Texas at Austin, Austin, TX, USA. ³Department of Molecular and Cell Biology, University of California Merced, Merced, CA, USA. ⁴Neuroscience Graduate Program, Brown University, Providence, RI, USA. ⁵Department of Molecular Pharmacology, Physiology and Biotechnology, Brown University, Providence, RI, USA. ⁶Center for Systems and Synthetic Biology, University of Texas at Austin, Austin, TX, USA.

⁷These authors contributed equally: Corey Frazer, Mae I. Staples. [✉]e-mail: Richard_Bennett@brown.edu

(see Extended Data Fig. 1). These TFs co-occupy similar genomic positions despite a paucity of DNA-binding motifs, many of which were defined using unbiased in vitro approaches²⁷ (Fig. 1d; Extended Data Fig. 1). This suggests that *C. albicans* cell fate-defining TFs are recruited to expanded DNA regulatory regions, at least in part, via protein–protein interactions.

C. albicans white-opaque TFs can form phase-separated condensates. We noted that seven of eight white-opaque TFs contain PrLDs as defined by prion-like amino acid composition (PLAAC) analysis⁴¹. Thus, Czf1, Efg1, Ssn6 and Wor1–Wor4 all contain at least one PrLD (Fig. 1e). PrLDs are intrinsically disordered, low-complexity domains that are rich in glutamine/asparagine residues yet contain few charged or hydrophobic residues. Although recognized for their ability to form self-templating amyloid fibrils, PrLDs can also increase the propensity for proteins to undergo LLPS^{42,43}.

To test whether white-opaque TFs undergo phase separation in vitro, we purified *C. albicans* Czf1, Efg1, Wor1 and Wor4 proteins from *Escherichia coli* as fusions with maltose-binding protein (MBP) (see Extended Data Fig. 2). Strikingly, each protein underwent LLPS upon proteolytic release from MBP (Fig. 2a). A chimera between the *C. albicans* Wor1 DNA-binding domain (DBD) and the *Candida maltosa* Wor1 PrLD was used for several of these experiments, as purified *CaCmWor1* was obtained in higher amounts than native *CaWor1* and the chimeric protein was functional in *C. albicans* white-opaque switching assays (see Fig. 4).

Efg1 formed liquid-like droplets at concentrations as low as 5 μM under physiological buffer conditions and without molecular crowding agents (Fig. 2b). Droplet–droplet fusion events were readily observed and droplet size increased with increasing Efg1 concentrations (Fig. 2a,b) but was inhibited by increasing salt concentrations (Fig. 2c). At high Efg1 and low salt concentrations, droplets showed less liquid-like behaviour and formed amorphous aggregates (Fig. 2c). Condensate formation was also observed with Czf1, Wor1 and Wor4, although the extent of liquid-like behaviour varied between TFs. Both Wor1 and Wor4 formed gel-like droplets that self-adhered to form chains, whereas Czf1 and Efg1 produced spherical droplets that continued to undergo liquid–liquid fusion events under identical conditions (Fig. 2a,b). We further probed the liquid-like properties of the TFs by treating pre-formed droplets with the aliphatic alcohol 1,6-hexanediol, which has been shown to disrupt weak hydrophobic interactions in phase-separated condensates^{44–46}. Efg1 droplets were completely dissolved by 10% 1,6-hexanediol whereas other condensates showed variable results. Czf1 and Wor1 were largely unaffected, whereas Wor4 showed reduced droplet size and number (see Extended Data Fig. 3a). We further examined Wor4 condensates by treating them with 10% 1,6-hexanediol before addition of TEV (tobacco etch virus)/5% poly(ethylene glycol) (PEG) and in this instance droplet formation

was essentially abolished. Treatment of condensates with the related compound 2,5-hexanediol, which does not dissolve liquid-like assemblies, did not generally disrupt droplets in any of these assays (see Extended Data Fig. 3a).

Notably, liquid droplets formed by one white-opaque TF supported co-compartmentalization with other network TFs. For example, using Efg1 as the bulk reagent, fluorescently labelled Efg1, Wor1, Wor4 and Czf1 were included at subphase-separating concentrations (37.5 nM). Upon TEV treatment, the bulk unlabelled Efg1 formed liquid droplets that incorporated each of the labelled TFs into condensates that continued to undergo droplet–droplet fusion (Fig. 2d). When treated with 10% 1,6-hexanediol, but not 2,5-hexanediol, these droplets readily dissolved, further indicating their liquid properties (see Extended Data Fig. 3b). TF co-compartmentalization also occurred when TFs other than Efg1 were used as the bulk reagent (see Extended Data Fig. 3c). These results show how condensates formed by a single *C. albicans* TF can promote heterotypic interactions between TFs.

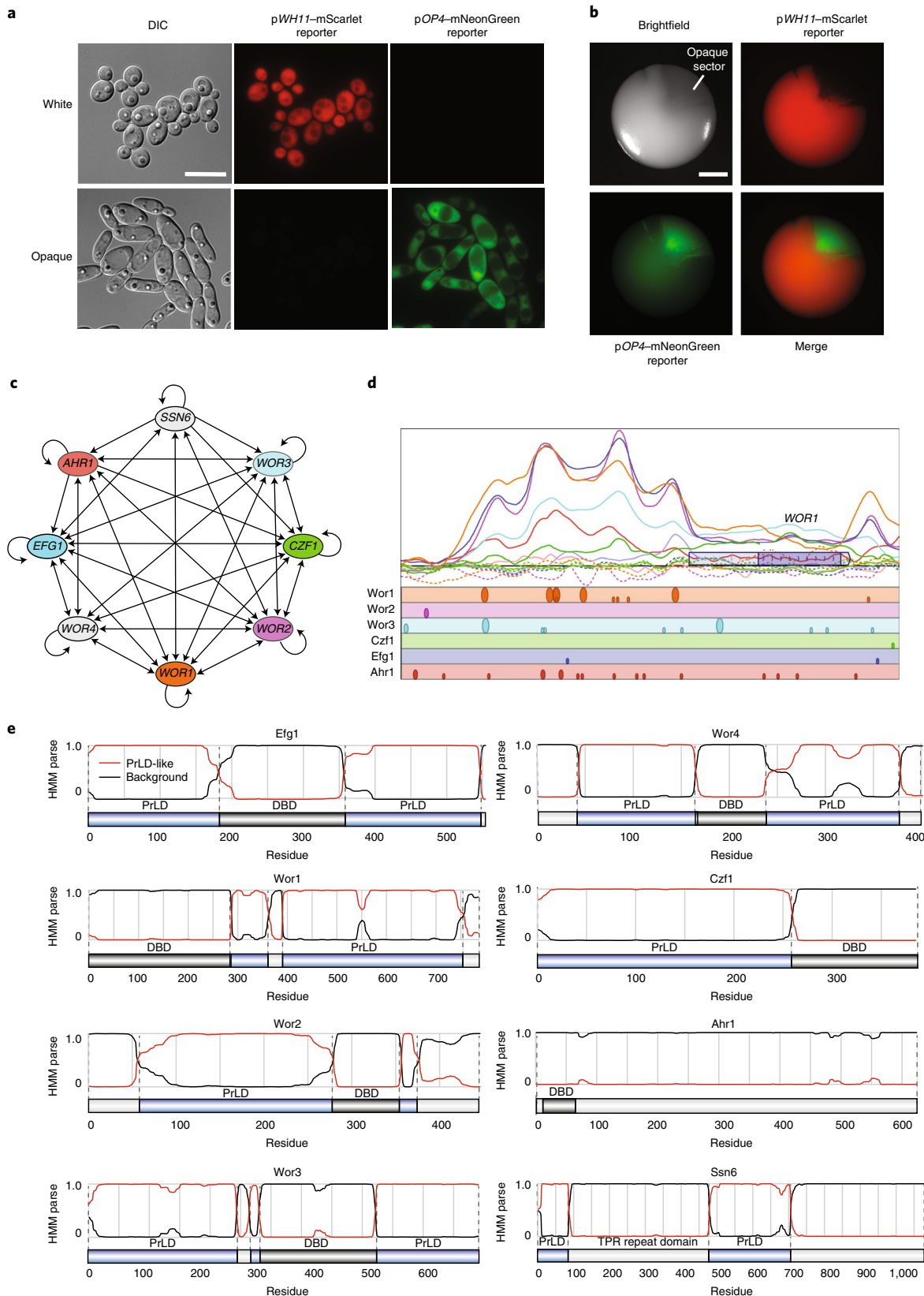
PrLDs promote LLPS by *C. albicans* white-opaque TFs. The contribution of PrLDs to phase separation of white-opaque TFs was determined. Efg1 contains N- and C-terminal PrLDs that flank an APSES DBD^{47,48}. Loss of either PrLD abolished the ability of Efg1 to phase separate under conditions where the native protein readily formed droplets (30 μM Efg1; Fig. 2e). Similar results were obtained with Czf1 and Wor4, where removal of PrLDs attenuated phase separation; removal of the single PrLD from Czf1 resulted in the formation of smaller droplets than the full-length protein whereas removal of both PrLDs from Wor4 abolished droplet formation (Fig. 2a,e). More subtle phenotypes were observed in Wor4 when only one PrLD was deleted; loss of the N-terminal PrLD reduced droplet formation, whereas removal of the C-terminal PrLD resulted in increased gelling (that is, formation of irregular assemblies that did not form larger droplets) (Fig. 2a,e). In the case of Wor1, deletion of the C-terminal PrLD still allowed the protein to form aggregate chains even at concentrations as low as 5 μM, although these aggregates were smaller than those formed by the native protein (Fig. 2a,e). The inclusion of DNA was also found to impact phase separation of TFs; Efg1 forms relatively small droplets at concentrations of 5–10 μM, yet the presence of *C. albicans* genomic DNA (gDNA) or phage lambda (λ) DNA enabled Efg1 to form larger droplets under the same conditions (Fig. 2f). This indicates that DNA can promote condensates formed by a *C. albicans* TF.

To examine homotypic and heterotypic interactions mediated by PrLDs, the DBD was replaced with green fluorescent protein (GFP; see Extended Data Fig. 4a) and TF recruitment into Efg1 condensates analysed. Efg1[N-GFP-C] was readily recruited into bulk Efg1 droplets, whereas removal of the N- or C-terminal PrLDs led to weak or no recruitment into droplets, respectively

Fig. 1 | The white-opaque transcriptional network in *C. albicans* is regulated by multiple TFs containing PrLDs. **a**, *C. albicans* cells can switch between two cell states with distinct colony and cellular morphologies. Representative images are shown for a strain expressing white-specific (*pWH11-mScarlet*) and opaque-specific (*pOP4-mNeonGreen*) reporters in both white and opaque cell states. Scale bar, 10 μm. **b**, White-opaque switching at the colony level. Image of a single *C. albicans* colony expressing white- and opaque-specific reporters after growth at 22 °C for 7 d on SCD medium. Image shows a representative white colony with an opaque sector. Scale bar, 1 mm. **c**, Transcriptional network regulating the opaque state in *C. albicans*. Arrows represent direct binding interactions for TFs to the regulatory region of a given gene based on ChIP-chip/ChIP-sequencing data. Model adapted from previous studies, see refs. ^{27–36}. **d**, Top: summary of ChIP-chip data for binding of network TFs to the *WOR1* promoter and ORF. Solid lines indicate TF binding and dotted lines indicate controls. ChIP-chip binding shown for Wor1 (orange), Wor2 (pink), Wor3 (blue), Czf1 (green), Efg1 (purple) and Ahr1 (red). The *WOR1* ORF is represented by a purple box and a lighter purple box represents the untranslated region. Bottom: positions of consensus DNA-binding sites for each TF. The large circles represent motif hits with >75% of the maximum score, medium circles represent motif hits with 50–75% of the maximum score and small circles represent motif hits with 25–50% of the maximum score. The ChIP enrichment plot was generated from data in refs. ^{27,30,36} and motif analysis performed using data from refs. ^{27,30}. **e**, PLAAC analysis to identify PrLDs. A hidden Markov model (HMM) is used to parse protein regions into PrLDs and non-PrLDs on the basis of their amino-acid composition. Relative position of PrLDs and DBDs is shown for the eight master TFs that regulate white-opaque identity in *C. albicans*.

(see Extended Data Fig. 4b). Similar results were obtained with Wor1, Wor4 and Czf1, where replacement of DBDs with GFP-generated chimeric proteins that could be readily recruited into Efg1 condensates (see Extended Data Fig. 4a,b). In the case of Wor4,

similar to Efg1, both the N- and C-terminal PrLDs were necessary for efficient recruitment into Efg1 droplets. These data show that PrLDs promote phase separation which allows for heterotypic interactions between white-opaque TFs.



PrLD-containing TFs form phase-separated condensates on single DNA molecules. TF condensate formation on single DNA molecules was examined using a ‘DNA curtain’ assay. Here, DNA is trapped on top of a fluid lipid bilayer with molecules tethered at one end and fluorescently labelled at the other end (Fig. 3a)^{49,50}. DNA molecules are extended by buffer flow and the lipid bilayer serves as a biomimetic surface that blocks non-specific adsorption of proteins and nucleic acids to the flowcell.

C. albicans Efg1 was examined in DNA curtain assays with the consensus binding motif for Efg1 (TGCAT)²⁷ represented 145 times in the 48.5-kb phage lambda genome used for these assays. MBP-Efg1 was pre-incubated with TEV protease and the mixture injected into flowcells containing pre-assembled DNA curtains. Efg1 binding resulted in the contraction of DNA molecules as measured by movement of the untethered, fluorescently labelled end towards the tethered end (Fig. 3b, top). Importantly, DNA compaction required both the DBD and the PrLDs of Efg1; injection of Efg1[N-GFP-C], which lacked the DBD, did not show detectable binding or contraction of DNA, whereas injection of Efg1ΔNC-GFP, which lacked both PrLDs, coated the DNA molecules but also failed to contract DNA (Fig. 3b).

Efg1 contracted DNA molecules almost completely to the barrier when using high (300 nM) or intermediate (50 nM) concentrations (Fig. 3c,d,g,h). In contrast, MBP-Efg1 that was not TEV treated (and thus unable to undergo LLPS) showed a significantly slower DNA contraction rate and a reduced average contraction length (Fig. 3c,d; $P < 0.0001$). Together, these data implicate both the DNA binding and phase-separation properties of Efg1 as important for driving the contraction of DNA molecules.

We next sought to determine whether PrLDs can promote homotypic or heterotypic interactions on single DNA molecules. In this case, DNA molecules were tethered at both ends to inhibit DNA contraction^{49,50} and MBP-TF fusions again TEV treated to remove MBP before injection. Full-length, unlabelled Efg1 was allowed to bind to the DNA before injection with TF-GFP fusions that lack their corresponding DBDs. We observed that both Efg1[N-GFP-C] and Wor1[GFP-C] rapidly accumulated in foci over the length of Efg1-coated DNA molecules (Fig. 3e), whereas Efg1[N-GFP-C] did not bind to DNA in the absence of native Efg1 (Fig. 3b). This shows that Efg1 and Wor1 can both be recruited into TF-DNA compartments via their PrLDs.

TFs function in the context of chromatin and we therefore assessed how nucleosomes impact DNA condensation. DNA curtains

were prepared with >10 nucleosomes deposited on to each DNA molecule and visualized using a fluorescent antibody against a human influenza haemagglutinin (HA) epitope on histone H2A^{51,52}. Efg1 caused contraction of nucleosomal DNA substrates, although this occurred at a significantly slower rate than that of naked DNA (Fig. 3f-h; $P = 0.001$), indicating that nucleosomes act as physical barriers to DNA binding and/or DNA compaction by Efg1. In support of this model, nucleosome-free DNA regions compacted more rapidly than nucleosome-dense regions of the same DNA substrate (see arrows, Fig. 3f).

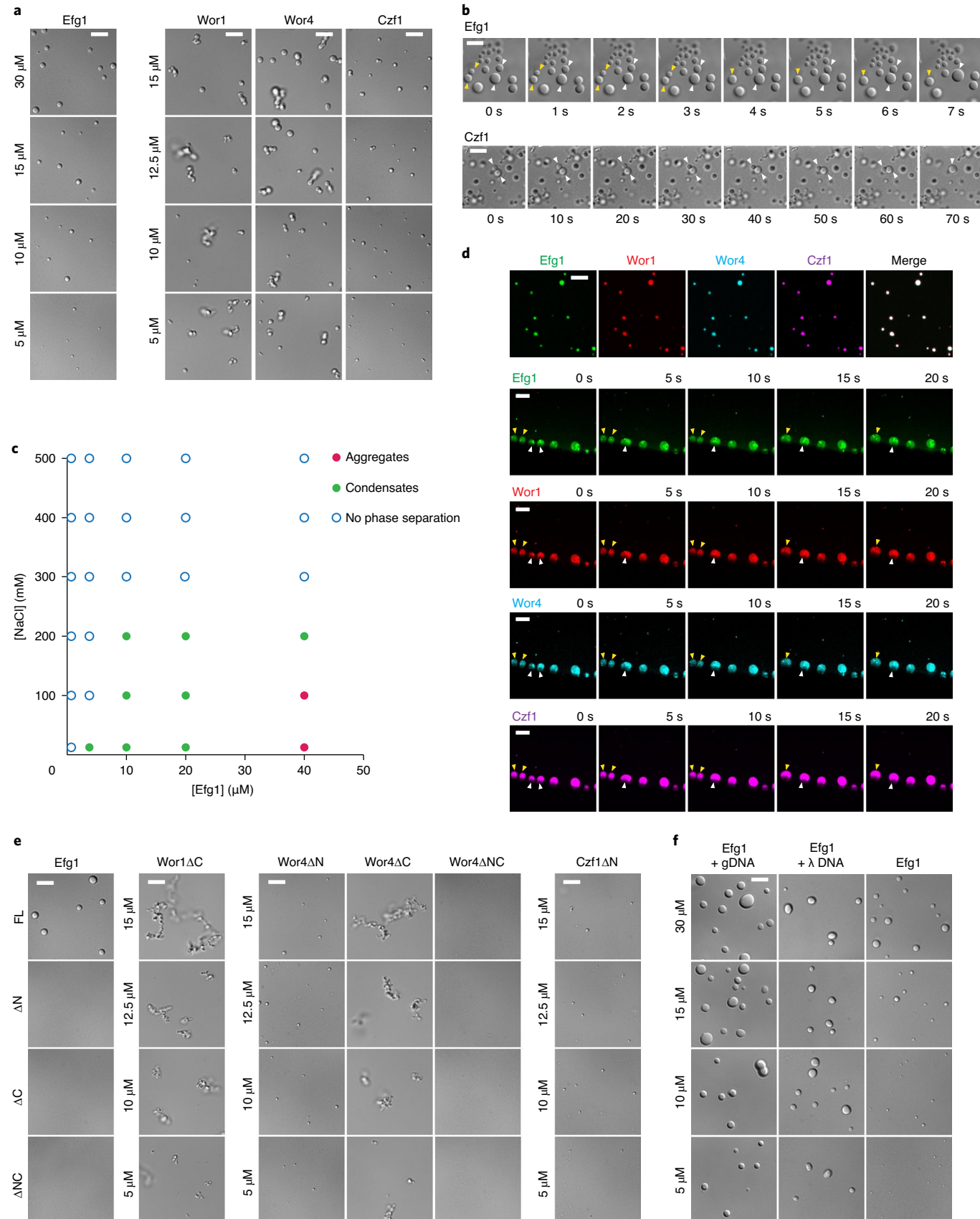
PrLDs are necessary for TF function in determining *C. albicans* white-opaque cell fate. The functional contribution of PrLDs to the regulation of *C. albicans* cell fate was tested by ectopic expression of mutant TFs and quantification of white-to-opaque switching. Induced expression of full-length TFs led to elevated frequencies of switching, as expected^{29–32,35}. Thus, whereas <2% of colonies showed stochastic white-to-opaque switching under non-inducing conditions, forced expression of WOR1, WOR4 or CZF1 resulted in 98%, 63% or 45% of white colonies showing to the opaque state, respectively (Fig. 4a-d). In contrast, ectopic expression of TFs lacking their respective PrLDs showed no increase in white-to-opaque switching over background (Fig. 4b-d).

Phase separation is promoted by multivalent interactions between residues in low complexity domains, with multiple weak interactions able to overcome the entropic cost of LLPS⁵³. Recent studies implicate a variety of intermolecular interactions in driving LLPS including patterned charged residues, hydrophobic residues and aromatic residues, with the latter shown to promote various π interactions^{43,54–57}. Glutamine residues can also enhance LLPS and promote the liquid-to-solid transition of condensates^{43,57}. To address whether these residues alter the functionality of a white-opaque TF, derivatives of the CmWor1 PrLD were tested including: (1) removal of negatively charged residues (DE-to-A mutant), (2) removal of positively charged residues (KR-to-G mutant), (3) substitution of aromatic residues (YF-to-S mutant) and (4) deletion of repetitive polyN/polyQ tracts (Δ PolyNQ) (Fig. 4e). Notably, both DE-to-A and YF-to-S mutants abolished Wor1 function in white-opaque switching, whereas KR-to-G and Δ PolyNQ mutants showed wild-type functionality (Fig. 4f). In the case of the DE-to-A mutant, we note this involved substitution of only 8 residues within the 312-residue PrLD. All Wor1 variants correctly localized in the nucleus as determined by fluorescence microscopy (Fig. 4g).

Fig. 2 | *C. albicans* white-opaque TFs undergo phase separation in vitro. **a**, Images of protein droplets formed by Efg1, Wor1 (CaCmWor1), Wor4 and Czf1. Assays performed in 10 mM Tris-HCl buffer, pH 7.4, 150 mM NaCl, at 22 °C after 30-min incubation with TEV. Wor1, Wor4 and Czf1 assays included 5% PEG-8000. Images represent a single experimental replicate, with assays carried out three times with similar results. Scale bar, 5 μ m. **b**, Time course of Efg1 (top) and Czf1 (bottom) undergoing droplet-droplet fusion events. White and yellow arrows indicate separate droplet fusion events. Droplets formed using 15 μ M of each TF in 10 mM Tris-HCl, pH 7.4, 150 mM NaCl. Samples were incubated at 22 °C with TEV added 30 min before imaging. Images represent a single time course, with assays repeated three times with similar results. Scale bar, 5 μ m. **c**, Phase diagram of Efg1 phase-separation events at the indicated salt and protein concentrations after TEV treatment at 22 °C. Condensates indicate formation of circular droplets. Aggregates indicate formation of clusters of droplets. **d**, Representative images of fluorescently labelled Efg1, Wor1 (CaWor1), Wor4 and Czf1 proteins compartmentalized within Efg1 condensates. Unlabelled Efg1 (15 μ M) was allowed to form condensates in the presence of each of the fluorescently labelled proteins (37.5 nM) in 10 mM Tris-HCl, pH 7.4, 150 mM NaCl. Proteins were pre-incubated at 22 °C with TEV for 30 min. DyLight NHS Ester labelling of the four proteins used fluors of 405, 488, 550 and 633 nm. Images represent a single experimental replicate, and assays were repeated three times with similar results. Scale bar, 5 μ m for compartmentalization and 20 μ m for droplet fusion events. Images are maximum z-stack projections. White and yellow arrows indicate separate droplet fusion events with images shown in 5-s intervals from a time range of 50–70 s over a total imaging time of 100 s. **e**, Phase-separation analysis of Efg1, Wor1, Wor4 and Czf1 in which PrLDs have been removed. Efg1 was used at 30 μ M whereas Wor1, Wor4 and Czf1 were present at the indicated protein concentrations. Proteins were pre-incubated with TEV for 30 min at 22 °C before analysis. Assays were performed in 10 mM Tris-HCl, pH 7.4, 150 mM NaCl and supplemented with 5% PEG-8000 for Wor1, Wor4 and Czf1. Images represent a single experimental replicate, with assays repeated three times with similar results. Scale bar, 5 μ m. FL, full-length protein; Δ N, Δ C or Δ NC, protein without N-terminal PrLD, C-terminal PrLD or both PrLDs, respectively. **f**, Images of Efg1 droplets formed with *C. albicans* gDNA, phage λ DNA and without addition of DNA. Assays performed in 10 mM Tris-HCl buffer, pH 7.4, 150 mM NaCl, at 22 °C after 30-min incubation with TEV. The gDNA was included at a final concentration of 50 nM and phage λ DNA was included at a final concentration of 9.4 nM. Images represent a single experimental replicate, with assays repeated twice with similar results. Scale bar, 5 μ m.

We also tested whether Wor1 could regulate cell fate if its PrLD were replaced with the PrLD of another TF. Substitution of the Wor1 PrLD with that from the white-to-opaque regulator Czf1 or

from TAF15, a mammalian FET family TF, generated chimeric proteins that were still fully functional in white-to-opaque switching (Fig. 4f). These experiments reveal that negatively charged residues



and aromatic residues in the PrLD are critical for Wor1 function, and that PrLDs from other TFs can substitute for the native PrLD despite lacking any substantial sequence homology.

Formation of *C. albicans* TF condensates at genomic loci in live cells. To determine whether *C. albicans* white–opaque TFs form condensates in a cellular environment, we tested their heterologous expression in a mammalian cell line that has been used for monitoring LLPS in vivo^{8,58}. In this system, U2OS cells containing ~50,000 copies of the Lac operator (LacO) are used to recruit proteins fused to the Lac repressor (LacI)^{8,59}. We tested expression of PrLDs from Efg1, Czf1, Wor1 or Wor4 fused to LacI–EYFP and found that each formed bright foci at the LacO array, as well as smaller puncta throughout the nucleus (Fig. 5a,b). These PrLDs generated structures at the LacO array that were visible by differential interference contrast (DIC) microscopy (Fig. 5b), suggesting that the mass density/refractive index of these assemblies distinguishes them from their environment, as observed with foci formed by human TFs⁸. Importantly, analysis of LacO-associated hubs showed that foci associated with *C. albicans* PrLDs were larger and brighter than foci formed by LacI without a PrLD, as well as larger than foci formed by Ahr1 which lacks a PrLD (Fig. 5c). This indicates that PrLD–PrLD interactions enhance protein recruitment to the LacO array. In addition, LacI fused to Efg1, Czf1, Wor1 or Wor4 PrLDs produced additional puncta throughout the nuclei, whereas LacI alone did not, establishing that these PrLDs can seed self-assembly independently of the LacO array (Fig. 5b).

To examine whether PrLD-mediated foci involved LLPS, U2OS cells were treated with 10% 1,6- or 2,5-hexanediol. When cells were treated with 1,6-hexanediol, foci formed by *C. albicans* PrLDs at LacO arrays shrank in both size and brightness, whereas smaller nuclear puncta disappeared completely with time scales ranging from 30 s (Wor4) to 6 min (Efg1) (Fig. 5d). Efg1-, Czf1-, Wor1- and Wor4-containing foci were not affected by 2,5-hexanediol to the same extent as 1,6-hexanediol (Fig. 5e), consistent with foci forming via liquid–liquid demixing.

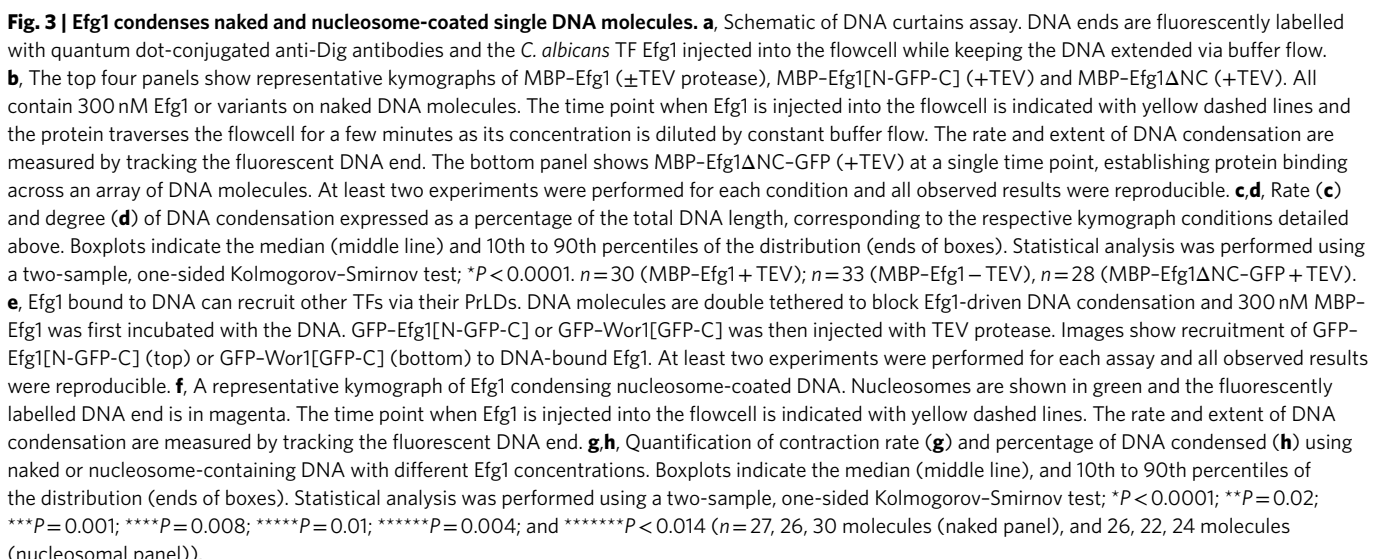
To dissect the amino-acid residues contributing to condensate formation, several Wor1 PrLD variants tested for functionality in *C. albicans* (Fig. 4) were evaluated for their properties in U2OS cells. We found that the KR-to-G and ΔPolyNQ PrLD variants that were functional in *C. albicans* showed similar condensate formation to the wild-type PrLD (Fig. 5f,g). In contrast, however, the non-functional DE-to-A variant showed no increase

in the size of the LacO-associated signal relative to LacI alone, and displayed significantly decreased fluorescence intensity at the array compared with the wild-type Wor1 PrLD and other variants (Fig. 5f,g). These results reveal that the Wor1 DE-to-A mutant that is defective in driving white-to-opaque switching in *C. albicans* cells is also defective in condensate formation in mammalian cells.

PrLDs mediate heterotypic interactions between *C. albicans* TFs in vivo. PrLDs from white–opaque TFs were tested for their ability to mediate homotypic and/or heterotypic interactions using U2OS cells. For these experiments, PrLDs were fused to EYFP–LacI or mCherry and co-expressed in U2OS cells containing the synthetic LacO array. Using this approach, PrLD–mCherry fusion proteins will show enrichment at the LacO array only if recruited by interactions with PrLD–LacI–EYFP proteins.

Given that PrLDs from white–opaque TFs increase the size of LacI foci formed at the LacO array (Fig. 5b), we predicted that homotypic interactions would occur between these PrLDs. In line with this, homotypic interactions were detected between the two Efg1–PrLD constructs, as well as between the two Czf1–PrLD constructs (Fig. 6a,b). Moreover, heterotypic interactions were detected between the Czf1, Wor1 and Wor4 PrLDs fused to LacI–EYFP and Efg1–PrLD–mCherry (Fig. 6a,b), indicative of interactions between PrLDs from different TFs. Recruitment via PrLDs was not limited to the LacO array because additional nuclear puncta were observed that contained both EYFP and mCherry signals (for example, see Efg1–Efg1 and Wor1–Efg1 interactions in Fig. 6a).

Potential interactions between *C. albicans* PrLDs and those in human TFs were also examined. The human FET TF family includes FUS and TAF15 which can form phase-separated condensates, as can Sp1 from the Sp/KLF TF family^{5–8}. Previously, the FUS–PrLD was shown to form heterotypic interactions with PrLDs from other FET family TFs but not with the Sp1–PrLD⁸. Interestingly, Efg1 PrLDs formed heterotypic interactions with the FUS–PrLD, as Efg1–PrLD–mCherry was recruited to FUS–PrLD–LacI–EYFP at the LacO array and these proteins also co-localized at other sites in the nucleus (Fig. 6b). In contrast, PrLDs from Czf1, Wor1 and Wor4 failed to interact with FUS and an Sp1–PrLD–fusion protein did not recruit Efg1– or Czf1–PrLD proteins (Fig. 6b). These results show that *C. albicans* PrLDs can promote co-assembly of fungal TF complexes, as well as support interactions between fungal TFs and a subset of their mammalian counterparts.



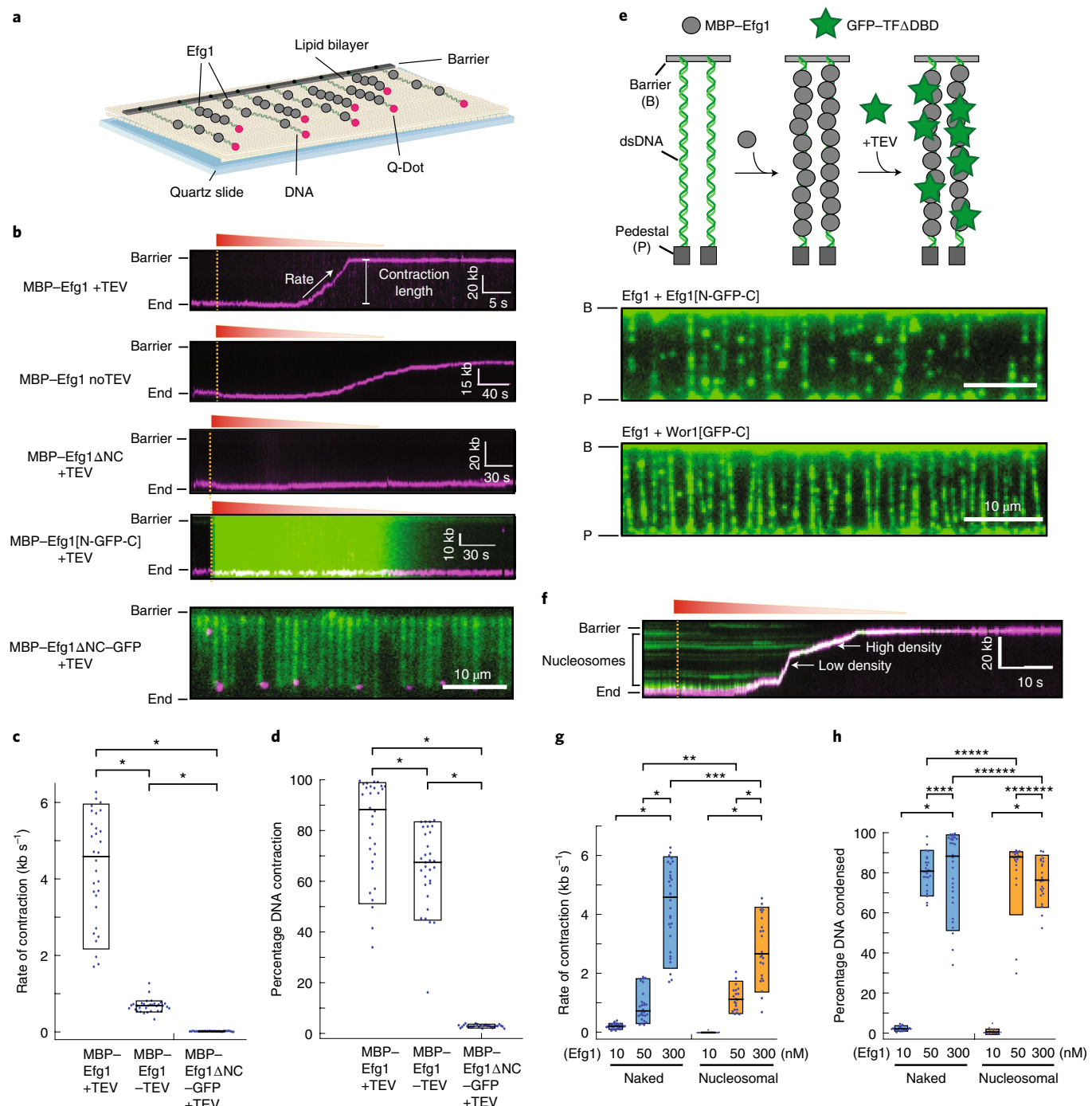
Finally, we tested whether the DE-to-A-substituted Wor1 PrLD that is defective in condensate formation (Fig. 5f,g) and white-opaque switching (Fig. 4f) could recruit other PrLDs to the LacO array in U2OS cells. Strikingly, this variant was completely defective in recruiting Efg1–PrLD–mCherry to the LacO array (Fig. 6c). This establishes that a mutant PrLD defective in phase separation is unable to co-recruit other TF PrLDs, and is consistent with a role for phase separation in the transcriptional control of fungal cell fate.

Discussion

How does a highly interconnected network of TFs regulate cell identity? This question is a clinically relevant one for *C. albicans*,

where transitions between cell states modulate interactions with its human host^{19–22}. In this study, we reveal that the TFs regulating the *C. albicans* white–opaque switch contain PrLDs that promote LLPS and propose that this is integral to their function in regulating fungal cell fate.

We demonstrate that *C. albicans* white–opaque TFs can form multifactorial condensates and show this both on single DNA molecules in vitro and in live eukaryotic cells. Critically, deletion or mutation of PrLDs blocks LLPS and the assembly of TF complexes, and concomitantly abolishes TF function. In particular, substitution of eight acidic residues within the Wor1 PrLD disrupted its function in *C. albicans* cells and also blocked condensate formation in mammalian cells. This is consistent with electrostatic interactions being



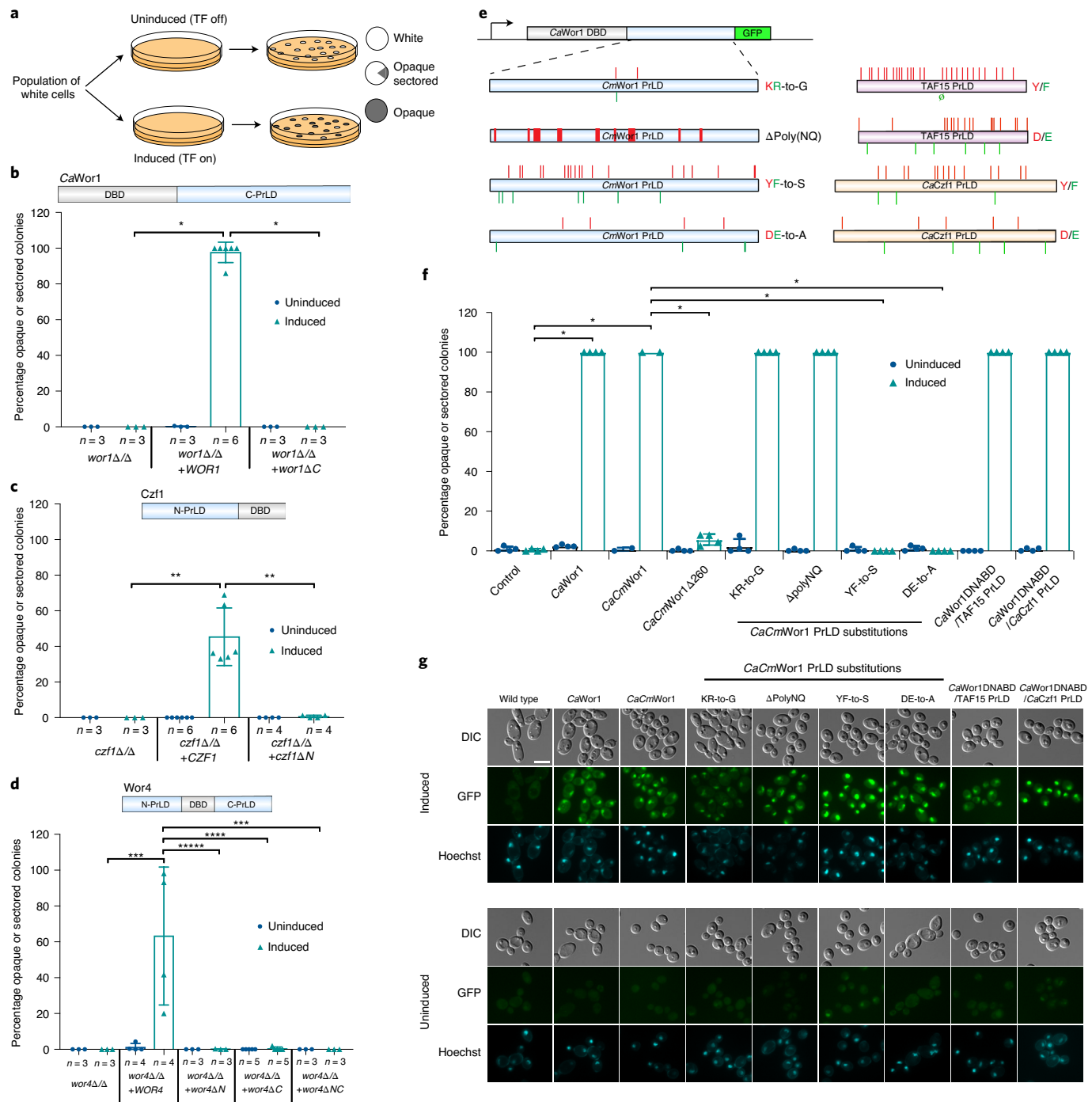


Fig. 4 | Deletion or mutation of PrLDs abolishes the function of *C. albicans* TFs in cell fate determination. **a**, Cell state switching assays. *C. albicans* white cells were analysed for the frequency of switching to the opaque state. White cells were plated for single colonies on control non-inducing medium or on inducing medium. Colony phenotypes were analysed after 7 d incubation at 22 °C. **b–d**, Effect of ectopic expression of *WOR1* (**b**), *CZF1* (**c**) or *WOR4* (**d**) variants from the *MAL2* promoter on white-to-opaque switching frequencies. In each case, TFs were expressed with or without the indicated N- or C-terminal PrLDs. Each TF was tested in the corresponding null mutant background (for example, *WOR1* variants were expressed in a strain that is a *wor1Δ/Δ* mutant). Values show the mean switching frequency in each strain and the error bars represent the s.d. Comparisons were performed between the full-length and mutant constructs under inducing conditions using a two-tailed, unpaired Student's *t*-test with Welch's correction. **P* < 0.0001; ***P* = 0.0010; ****P* = 0.0463; *****P* = 0.0470; ******P* = 0.0465. **e**, The *C. albicans* *Wor1* DBD was fused to the PrLD of *C. maltosa* *Wor1* with the indicated amino-acid substitutions. Also shown is the arrangement of YF and DE residues in the PrLDs of human TAF15 and *C. albicans* *Czf1* tested for their ability to functionally replace the *Wor1* PrLD. **f**, White-to-opaque switching frequency of indicated constructs expressed from the *MET3* promoter in a strain containing wild-type *WOR1*. Colony phenotypes were analysed after 7 d at 22 °C. Statistical comparisons were performed between strains using a two-tailed, unpaired Student's *t*-test with Welch's correction. **P* < 0.0001. Control is the parental strain with no plasmid integrated. **g**, Relative GFP expression levels of *CaCmWor1* PrLD substitutions and replacements. Images representative of two independent experimental replicates that showed the same result. GFP and Hoechst histograms are set to equivalent levels. Scale bar, 5 μm.

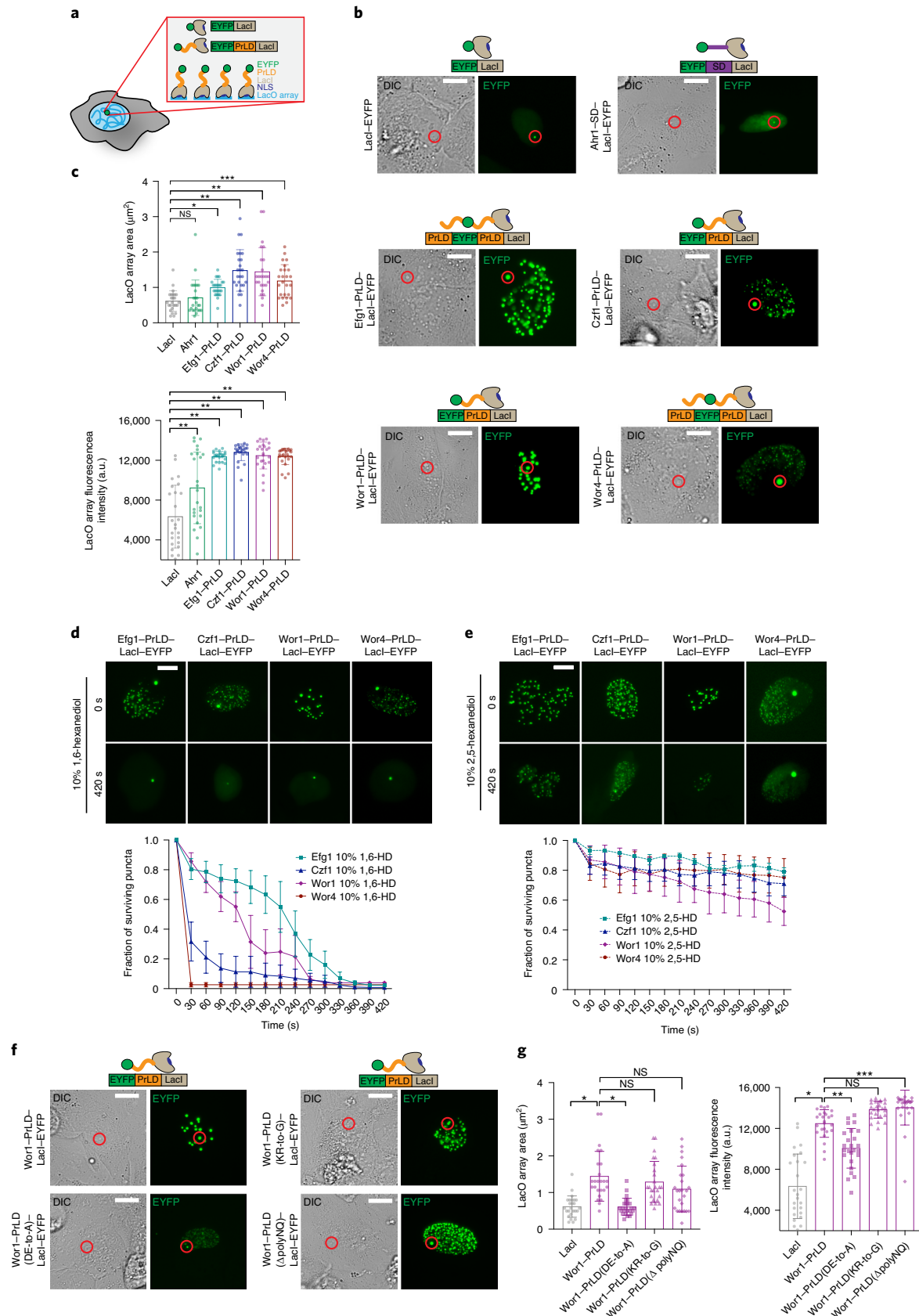


Fig. 5 | C. albicans PrLDs enable the formation of phase-separated condensates at a genomic array in live cells. **a**, Schematic of mammalian U2OS cells containing a LacO array used to recruit LacI or LacI-PrLD fusion proteins. **b**, Representative fluorescence microscopy and DIC images of U2OS cells containing the LacO array (indicated with a red circle) bound by the LacI-EYFP control, or by Ahr1-SD-Laci-EYFP, Efg1-PrLD-Laci-EYFP, Czf1-PrLD-Laci-EYFP, Wor1-PrLD-Laci-EYFP or Wor4-PrLD-Laci-EYFP. SD, structured domain. Scale bars, 10 µm. Note that the PrLD from *C. maltosa* Wor1 was used in these experiments (see Methods). **c**, Quantification of average size (top) and fluorescence intensity (bottom) of the LacO array bound by LacI-EYFP, Ahr1-SD-Laci-EYFP, Efg1-PrLD-Laci-EYFP, Czf1-PrLD-Laci-EYFP, Wor1-PrLD-Laci-EYFP and Wor4-PrLD-Laci-EYFP. Fluorescence intensity calculated after subtraction of the background signal in the LacI-EYFP control. Values show the mean area and fluorescence intensity at the LacO array, and error bars show the s.d. Statistical analysis was performed using ordinary one-way ANOVA with Dunnett's multiple-comparison test, in which the mean value for each construct was compared with the mean for the LacI control. *P=0.0261; **P<0.0001; ***P=0.0003; NS, not significant (n=25, with images analysed from 25 individual cells for each construct). Experiments were repeated at least three times with similar results. a.u., arbitrary units. **d,e**, Representative fluorescence microscopy images of Efg1, Czf1, Wor1 and Wor4 foci in U2OS cells containing a LacO array before and after treatment with 10% 1,6-hexanediol (HD) (**d**) or 10% 2,5-hexanediol (**e**). Scale bars, 10 µm. Error bars represent the s.e.m. (n=3 for each construct in each condition tested, with cells analysed from at least three separate experiments with similar results). Images of cells 420 s after treatment have been enhanced for brightness for better representation of the remaining puncta in the nucleus. **f**, Representative fluorescence microscopy and DIC images of U2OS cells containing the LacO array (indicated with red circle) bound by wild-type Wor1-PrLD-Laci-EYFP or by the indicated Wor1-PrLD-Laci-EYFP variants. Scale bars, 10 µm. **g**, Quantification of average size (left) and fluorescence intensity (right) of the LacO array bound by the wild-type Wor1-PrLD-Laci-EYFP or each Wor1-PrLD-Laci-EYFP variant. Fluorescence intensity calculated after subtraction of the background signal in the LacI-EYFP control. Values show the mean area and fluorescence intensity at the LacO array, and error bars are the s.d. Statistical analysis was performed using ordinary one-way ANOVA with Dunnett's multiple-comparison test, in which the mean value for each construct was compared with the mean for the wild-type Wor1 control. *P<0.0001; **P=0.0001; ***P=0.0204 (n=25, with images analysed from 25 individual cells for each construct). Experiments were repeated at least twice with similar results.

an important driver of LLPS in intrinsically disordered regions, including those of mammalian TFs^{43,54,56,57}. Wor1 function is therefore predicted to be highly sensitive to phosphorylation events that introduce additional negative charges, aligning with other intrinsically disordered regions where phosphorylation modulates LLPS⁶⁰. It is also striking that the Wor1 PrLD can be substituted for PrLDs from other TFs (either fungal or mammalian) and its functional role retained, indicating that some PrLDs are interchangeable despite no clear conservation between their primary sequences.

A phase-separation model for TFs in regulating white–opaque cell fate is consistent with previous studies in *C. albicans*. First, the occupancy of white–opaque TFs at a given locus correlates with the number of different TFs bound to that locus²⁷, suggesting that cooperative interactions increase TF recruitment to the DNA. Second, multiple white–opaque TFs bind to highly overlapping positions in the genome despite a paucity of DNA-binding motifs (see Fig. 1), further suggesting that TFs are recruited, at least in part, by protein–protein interactions²⁷. Third, the white–opaque switch is extremely sensitive to perturbations in TF levels including those of *WOR1* (ref. ⁶¹), consistent with the threshold effects that accompany phase-separation events⁶². These studies support a model whereby LLPS enables co-recruitment of TFs to key regulatory regions in

the *C. albicans* genome. In mammalian cells, TFs have been shown to activate transcription by recruiting RNA polymerase II, cofactors and mediator into complex condensates^{3,7,8,58,63,64}. It should be noted, however, that the precise interrelationship of TFs, condensate formation and gene activation remains to be determined, with some studies indicating that transcription is driven by transient complexes rather than the formation of stable, phase-separated condensates^{58,65}.

Finally, we highlight parallels between the TRN regulating white–opaque fate with other TRNs both in *C. albicans* and in mammals. For example, the biofilm TRN in *C. albicans* exhibits extensive genetic interactions between multiple TFs^{66,67}, many of which also contain PrLDs. We therefore predict that PrLD–PrLD interactions similarly contribute to the regulation of biofilm formation, and that inhibition of these interactions could represent a new approach for treatment of *C. albicans* infections. Close parallels with mammalian TRNs are also noted where high concentrations of TFs and cofactors can assemble at ‘super-enhancers’, and where these elements are integral to the control of cell identity^{3,9,11,14,63}. As with the *C. albicans* white–opaque TRN, super-enhancers are characterized by their unusually large size and sensitivity to perturbation^{9,11}. We therefore propose a conserved role for LLPS of TFs at ‘super-enhancer-like’

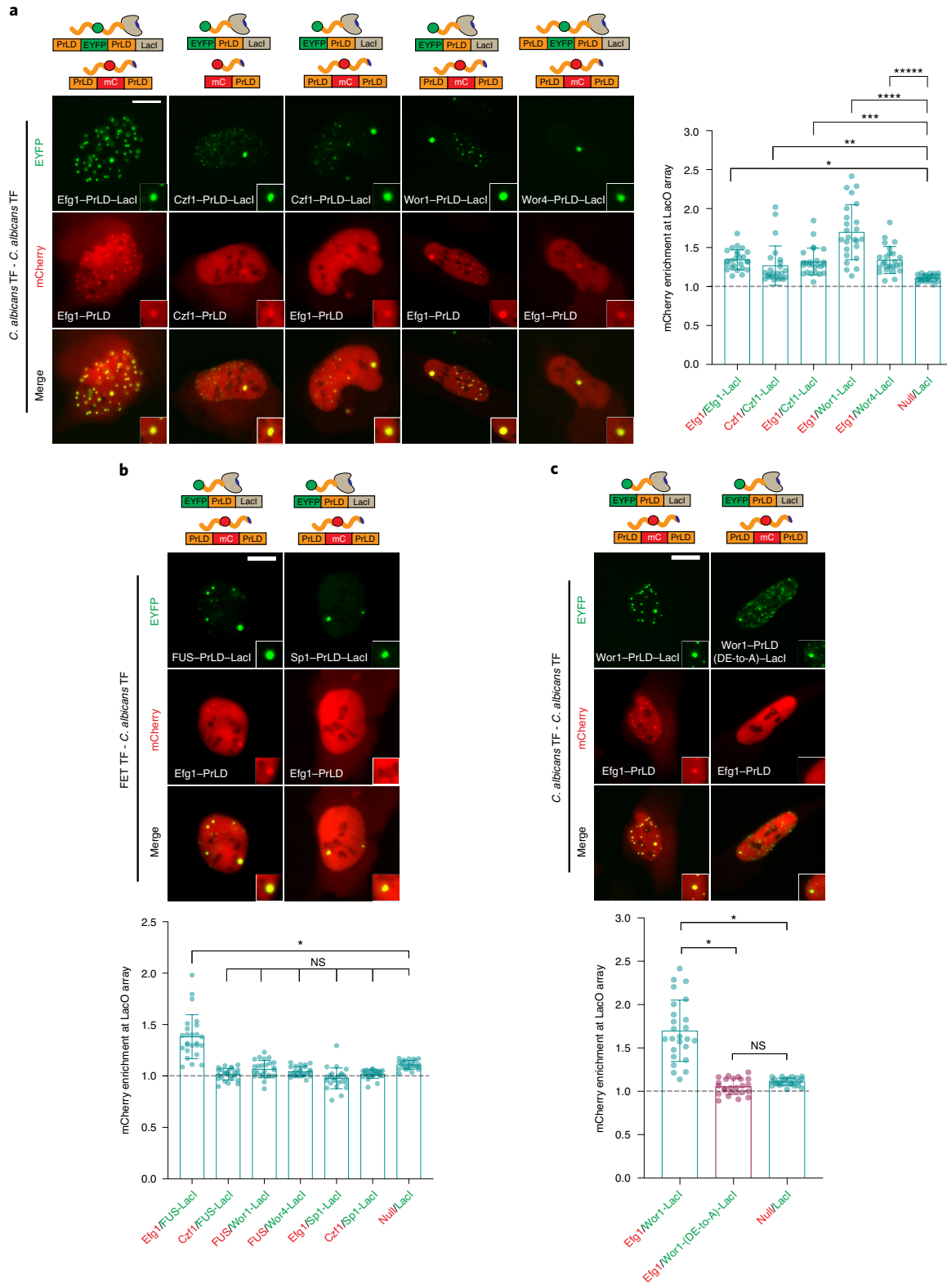
Fig. 6 | Condensates formed at a LacO array in U2OS cells involve both homotypic and heterotypic PrLD-PrLD interactions. **a**, Left, fluorescence microscopy images of *C. albicans* PrLD-Laci-EYFP and PrLD-mCherry constructs co-expressed in U2OS cells containing a LacO array. Right, quantification of mCherry-PrLD enrichment at the LacO array when bound by different PrLD-Laci-EYFP proteins. Enrichment defined as maximum intensity at the LacO array divided by average intensity directly outside the array. Null construct refers to mCherry alone when not fused to a PrLD. Enrichment >1 suggests that PrLD-PrLD interactions occur at the array. Data show the mean enrichment values and error bars are the s.d. Statistical analysis was performed using ordinary one-way ANOVA with Dunnett's multiple-comparison test, in which the mean enrichment value was compared with that for the control Null/Laci construct. P values are reported for mean values relative to that for the Null/Laci control: *P=0.0006; **P=0.0370; ***P=0.0027; ****P<0.0001; *****P=0.0008 (n=25 for each construct, with images analysed from 25 individual cells, and experiments repeated at least three times with similar results). Scale bars, 10 µm. Note that the PrLD from *C. maltosa* Wor1 was used in all U2OS cell experiments. **b**, Top, fluorescence microscopy images of FET TF family PrLD-Laci-EYFP and *C. albicans* PrLD-mCherry constructs co-expressed in U2OS cells containing a LacO array. Bottom, quantification of mCherry-PrLD enrichment at the LacO array when bound by different FET PrLD-Laci-EYFP proteins (see **a** and Methods). Data show the mean values and error bars are the s.d. Statistical analysis was performed using ordinary one-way ANOVA with Dunnett's multiple-comparison test in which the mean value was compared with that for the Null/Laci control. P values are reported for mean values greater than that for the Null/Laci construct: *P<0.0001 (n=25 for each construct, with images analysed from 25 individual cells, and experiments repeated at least three times with similar results). Scale bars, 10 µm. **c**, Top, fluorescence microscopy images of different Wor1 PrLD-Laci-EYFP and Efg1 PrLD-mCherry constructs co-expressed in U2OS cells containing a LacO array. Bottom, quantification of mCherry-PrLD enrichment at the LacO array when bound by either wild-type Wor1 or Wor1-PrLD(DE-to-A) proteins fused to Laci-EYFP constructs (see **a** and Methods). Data show the mean values and error bars are the s.d. Statistical analysis was performed using ordinary one-way ANOVA with Dunnett's multiple-comparison test. *P<0.0001 (n=25 for each construct, with images analysed from 25 individual cells, and experiments repeated at least twice with similar results). Scale bars, 10 µm.

regulons and that mechanisms of cell fate determination are shared from fungi to mammals.

Methods

Motif analysis. Motif analysis was performed using MochiView⁶⁸ and previously published position-specific affinity matrices (PSAMs) and position-specific weight matrices (PSWMs). Briefly, the regions flanking the genes shown in

Fig. 1d and Extended Data Fig. 1 were scanned for partial or complete matches to the Wor1, Wor2, Wor3, Czf1 and Efg1 PSAMs, which were derived from mechanically induced trapping of molecular interactions (MITOMI 2.0) in vitro binding data^{27,30}, and the Ahr1 PSWM that was derived from chromatin immunoprecipitation–DNA microarray (ChIP-chip) data²⁷. Motif hit scores were then binned based on their percentage of the maximum possible score for each motif (1.0 for MITOMI-derived PSAMs and 7.37 for the ChIP-chip-derived Ahr1 PSWM).



Plasmid construction. *AHR1*, *EFG1*, *CZF1*, *WOR1* and *WOR4* ORF sequences were codon optimized for expression in *E. coli*. These synthetic ORFs were cloned into pRB1B-MBP/THMT^{7,69} (pRB523) using NdeI/XhoI to create plasmids pRB515, pRB514, pRB516, pRB512 and pRB549, respectively. A chimeric *WOR1* construct was generated by combining the DBD of *C. albicans* *WOR1* with the PrLD of *C. maltosa* *WOR1*. The *CaWOR1* DBD was PCR amplified from pRB512 using oligos 4260/4261 and the *CmWOR1* PrLD was amplified from a codon-optimized sequence cloned into pUC57 (pRB791, Gene Universal) using oligos 4268/4269. A PCR fusion product between *CaWOR1*-DBD and *CmWOR1*-PrLD was generated using oligos 4260/4269 by splicing by overlap extension (SOE)-PCR⁷⁰ and cloned into pRB523 with NdeI/XhoI to create pRB838.

PrLD deletion plasmids for bacterial expression were constructed by PCR-amplifying fragments of the full-length *E. coli*-optimized ORFs and cloning into pRB1B-MBP using NdeI/XhoI: the pMBP-WOR1ΔC plasmid (pRB592) was created by amplifying the *WOR1* DBD (corresponding to amino acids 1–321) from pRB512 using oligos 3890/3891; the pMBP-CZF1ΔN plasmid (pRB596) was created by amplifying the DBD of *CZF1* (corresponding to amino acids 260–385) from pRB516 using oligos 3894/3895; the pMBP-EFG1ΔN plasmid (pRB594) was created by amplifying the DBD and C-terminal PrLD (corresponding to amino acids 181–554) from pRB514 using oligos 3896/3813; the pMBP-EFG1ΔC plasmid (pRB593) was created by amplifying the N-terminal PrLD and DBD of *EFG1* (corresponding to amino acids 1–356) from pRB514 using oligos 3812/3893; the pMBP-EFG1ΔNC plasmid (pRB595) was created by amplifying the *EFG1* DBD (corresponding to amino acids 181–356) from pRB514 using oligos 3892/3893; the pMBP-WOR4ΔN plasmid (pRB597) was created by amplifying the DBD and C-terminal PrLD (corresponding to amino acids 165–401) of *WOR4* from pRB549 using oligos 3896/3897; the pMBP-WOR4ΔC plasmid (pRB598) was created by amplifying the N-terminal PrLD and DBD of *WOR4* (corresponding to amino acids 1–246) from pRB549 using oligos 3898/3899; and the pMBP-WOR4ΔNC plasmid (pRB588) was created by amplifying the DBD of *WOR4* (corresponding to amino acids 165–246) from pRB549 using oligos 3896/3899.

The pMBP-GFP-PrLD fusions for *WOR1*, *EFG1*, *CZF1* and *WOR4* were constructed so that GFP replaces the DBD, using the same PrLD regions described above. To create the pMBP-WOR1[GFP-C] plasmid (pRB719), the C-terminal PrLD of *WOR1* was PCR amplified with oligos 4059/4060 from pRB512 and GFP was PCR amplified from pSJS1488 (a gift from S. Sandler, University of Massachusetts, Amherst) with oligos 4057/4058. The two fragments were combined using SOE-PCR with oligos 4057/4060, and the product cloned into pRB1B-MBP with NdeI/XhoI. The insert of pMBP-EFG1[N-GFP-C] (pRB717) was created by first PCR amplifying three overlapping fragments: N- and C-terminal *EFG1* PrLDs were amplified from pRB514 using oligos 4051/4052 and 4055/4056, respectively, and GFP was amplified from pRB690 using 4053/4054. The N-terminal PrLD was fused to GFP using SOE-PCR with oligos 4051/4054 and the C-terminal PrLD was fused to GFP by SOE-PCR using oligos 4053/4056. The former PCR product was digested with NdeI/MfeI and the latter product with MfeI/XhoI, and both cloned into pRB1B-MBP digested with NdeI/XhoI. The pMBP-EFG1[N-GFP] plasmid (pRB883) was created by PCR amplifying the N-terminal PrLD of *EFG1* and GFP from pRB717 using oligos 4455/4456, digesting with NheI/XhoI and cloning into pRB523. The pMBP-EFG1[GFP-C] plasmid (pRB885) was created by PCR amplifying GFP and the C-terminal PrLD of *EFG1* from pRB717 using oligos 4457/4056, and cloning into pRB523 with NheI/XhoI. The pMBP-CZF1[N-GFP] plasmid (pRB919) was created by SOE-PCR fusion of the *CZF1* N-terminal PrLD amplified from pRB516 (oligos 4466/4534) with GFP amplified from pRB690 (oligos 4458/4464). Fusion PCR was conducted using oligos 4466/4464. The PCR product was cloned into pRB1B-MBP with NheI/XhoI. The pMBP-WOR4[N-GFP-C] plasmid (pRB887) insert was created by SOE-PCR of three fragments: the *WOR4* N-terminal PrLD amplified from pRB549 (oligos 4460/4461), GFP from pRB690 (oligos 4458/4459) and the *WOR4* C-terminal PrLD from pRB549 (oligos 4462/4463). Fusion PCR was conducted using oligos 4460/4463 and the product cloned into pRB1B-MBP with NheI/XhoI. The pMBP-WOR4[N-GFP] plasmid (pRB889) was generated by SOE-PCR of two fragments using oligos 4460/4464. The N-terminal PrLD was PCR amplified from pRB549 (oligos 4460/4461) and GFP amplified from pRB690 (oligos 4458/4464). The resulting fusion product was cloned into pRB523 using NheI/XhoI. The pMBP-WOR4[GFP-C] plasmid (pRB891) was created by SOE-PCR of two fragments with oligos 4465/4463. GFP was PCR amplified from pRB690 (oligos 4465/4459) and the C-terminal PrLD was amplified from pRB549 (oligos 4462/4463). The fusion product was cloned into pRB523 with NheI/XhoI. The pMBP-GFP plasmid (pRB723) was created by PCR amplifying GFP from pRB690 (oligos 4122/4123), which was cloned into pRB523 with NheI/XhoI.

For inducible expression of white-opaque TF regulators in *C. albicans*, ORFs were cloned under the control of the *MAL2* or *MET3* promoter. The pMAL2-WOR1 plasmid (pRB488) was created by PCR amplifying the *MAL2* promoter (oligos 3455/3456) and the *WOR1* ORF (oligos 3457/3458) and assembling these fragments by SOE-PCR. The resulting PCR product was cloned into pSFS2A⁷¹ using ApaI/XhoI. To create a plasmid with the *MAL2* promoter driving *CaWOR1*DBD/*CmWOR1*PrLD expression (pRB843), the insert was assembled by SOE-PCR. The *CaWOR1* DBD was PCR amplified from *C. albicans* SC5314 gDNA (oligos 4155/4156) and the *Cm*PrLD was amplified from *C. maltosa* Xu316 gDNA

(oligos 4368/4369). Fragments were fused by PCR (oligos 4155/4369) and cloned into pRB505 (pMAL2-EFG1-myc) with ApaI/XmaI. The plasmid pRB505 was constructed by PCR amplifying pMAL2 (oligos 3357/3358), the *EFG1* ORF (oligos 3541/3542) and a myc tag sequence from pMG1905 (ref. ⁷²) (oligos 3539/3540) and cloning the three PCR fragments into pSFS2A with KpnI/BamHI. Additional pMAL2-regulated constructs were cloned into pRB505 as ApaI/XmaI fragments; *WOR1*ΔC was PCR amplified from pRB488 (oligos 4155/4156) to create pRB760, *CZF1* was amplified from pNIM1-CZF1 (a gift from J. Morschhauser, University of Wurzburg) (oligos 4009/4011) to create pRB652, *CZF1*ΔN was amplified from pNIM1-CZF1 (oligos 4010/4011) to create pRB653, *WOR4* was amplified from pRB605 (pNIM1-WOR4) (oligos 4157/4158) to create pRB755, *WOR4*ΔN was amplified from pRB605 (oligos 4158/4159) to create pRB757, *WOR4*ΔC was amplified from pRB605 (oligos 4157/4160) to create pRB758 and *WOR4*ΔNC was amplified from pRB605 (oligos 4159/4160) to create pRB770.

The pMET3-*CaWOR1*-GFP plasmid (pRB1305) was created by a three-way ligation between the *WOR1* ORF amplified from pRB488 using oligos 5778/5785 and digested with XmaI/KpnI, GFP amplified from pRB137 using oligos 5789/5790 and digested with KpnI/HindIII, and pRB157 digested with XmaI/HindIII. The pMET3-*CaWOR1*DBD/*CmWOR1*PrLD-GFP plasmid (pRB1307) was created by a three-way ligation between *CaWOR1*DBD/*CmWOR1*PrLD amplified from pRB843 using oligos 5778/5786 and digested with XmaI/KpnI, GFP amplified from pRB137 using oligos 5789/5790 and digested with KpnI/HindIII, and pRB157 digested with XmaI/HindIII. The pMET3-*CaWOR1*DBD/*CmWOR1*PrLDΔ260 plasmid (pRB1443) insert (consisting of DNA encoding the DBD and 52 amino acids of the PrLD) was amplified from pRB843 using oligos 5778/6222 and cloned into pRB1309 using KpnI/XmaI. The plasmid pRB1309 was constructed identically to pRB1305 except with the *CZF1* ORF amplified from pRB1142 using oligos 5781/5787. The pMET3-*CaWOR1*DBD/*CmWOR1*PrLD(KR-to-G)-GFP (pRB1489) insert was created by SOE-PCR of the DBD of *CaWOR1* from pRB1442 using oligos 5778/6234 and the PrLD of *CmWOR1* with KR-to-G substitutions amplified from pRB1455 using oligos 4368/5786. Note that PrLD substitutions were created using the endogenous *CmWOR1*PrLD sequence, with the residues in question substituted to the most common codon for the amino acid replacements. PCR fusion was conducted using oligos 5778/5786 and the resulting fragment cloned into pRB1309 using XmaI/KpnI. The pMET3-*CaWOR1*DBD/*CmWOR1*PrLD(ΔpolyNQ)-GFP plasmid (pRB1491) was created by SOE-PCR of the *CaWOR1*DBD, as above, with the *CmWOR1*PrLD amplified from pRB1459, in which all stretches of three or more glutamine and/or asparagine residues were deleted, using oligos 6236/6237. PCR fusion was conducted using oligos 5778/6237 and the resulting fragment cloned into pRB1309 using XmaI/KpnI. The pMET3-*CaWOR1*DBD/*CmWOR1*PrLD(YF-to-S)-GFP plasmid (pRB1495) was created by SOE-PCR of the *CaWOR1*DBD as described above, and the *CmWOR1*PrLD containing YF-to-S substitutions was amplified from pRB1457 using oligos 4268/6235. PCR fusion was conducted using oligos 5778/6235 and the resulting insert cloned into pRB1309 using XmaI/KpnI. The pMET3-*CaWOR1*DBD/*CmWOR1*PrLD(DE-to-A)-GFP plasmid (pRB1424) was constructed by SOE-PCR of the *CaWOR1*DBD as described above, and the PrLD of *CmWOR1* containing DE-to-A substitutions amplified from pRB1242 using oligos 4368/6125. PCR fusion was conducted using oligos 5778/6125 and cloned into pRB1309 using XmaI/KpnI. The pMET3-*CaWOR1*DBD/TAF15PrLD plasmid (pRB1485) was constructed by SOE-PCR using the *CaWOR1*DBD amplified as described above, and the PrLD of *human TAF15* amplified from pRB1210 using oligos 6248/6249. PCR fusion was conducted using oligos 5778/6249 and the resulting product digested with XmaI/KpnI and ligated into pRB1309. The pMET3-*CaWOR1*DBD/*CaCZF1*PrLD-GFP plasmid (pRB1487) was created by SOE-PCR. The *CaWOR1* DBD was amplified as above, and the *CaCZF1* PrLD was amplified from pRB1309 using oligos 6250/6251. PCR fusion was conducted using oligos 5778/6251 and the resulting insert cloned into pRB1309 using KpnI/XmaI.

Plasmids for the expression of *C. albicans* TF PrLDs with EYFP/LacI or mCherry in U2OS cells were constructed using sequences codon optimized for expression in *E. coli* (as *C. albicans* CUG codons would be mistranslated as leucine in U2OS cells). The pEYFP-EFG1-PrLD-LacI plasmid (pRB1222) was constructed by fusion PCR of three fragments; the N-terminal PrLD of *EFG1* was PCR amplified from pRB514 (oligos 5578 and 5579), EYFP was amplified from pRB1208 (oligos 5580/5581) and the C-terminal PrLD of *EFG1* was amplified from pRB514 (oligos 5578/5583). SOE-PCR was conducted on the three fragments using oligos 5578/5583 and the resulting product cloned into pRB1208 with NheI/BspEI. To create pEYFP-AHR1-LacI (pRB1503) the ORF of *AHR1* lacking the DBD was amplified using oligos 6269/6270 from pRB515, and the insert digested using BsrGI/XmaI and ligated into pRB1209 digested with BsrGI/BspEI. The pEYFP-*CmWOR1*-PrLD-LacI plasmid (pRB1410) was created by amplification of the *CmWOR1*PrLD from pRB838 using oligos 6117/6118 and cloned into pRB1208 with BsrGI/BspEI. The pEYFP-*CmWOR1*PrLD(DE-to-A)-LacI plasmid (pRB1501) was created by PCR amplifying the *CmWOR1*PrLD with DE-to-A substitutions from pRB1461 using oligos 6244/6245, and cloned into pRB1208 with BsrGI/BspEI. The pEYFP-*CmWOR1*PrLD(KR-to-G)-LacI plasmid (pRB1497) was created by PCR amplifying the *CmWOR1*PrLD with KR-to-G substitutions from pRB1456 using oligos 6240/6241, and cloning into pRB1208 using BsrGI/BspEI. The pEYFP-*CmWOR1*PrLD(ΔpolyNQ)-LacI plasmid (pRB1499) was

created by PCR amplifying the *CmWOR1* PrLD from pRB1460, where all stretches of DNA encoding three or more asparagine and/or glutamine residues were deleted, using oligos 6242/6243, and cloning the insert into pRB1209 with BsrGI/BspEI. The pEYFP-CZF1-PrLD-LacI plasmid (pRB1216) was constructed by PCR amplifying the CZF1 PrLD from pRB516 (oligos 5575/5576), and cloning into pRB1208 with BsrGI/BspEI. The pEYFP-WOR4-PrLD-LacI plasmid (pRB1266) was constructed by fusion of the N-terminal WOR4 PrLD (PCR amplified from pRB549 with oligos 5671/5672), EYFP (amplified from pRB1208 with oligos 5673/5674) and the C-terminal WOR4 PrLD (amplified from pRB549 with oligos 5675/5676). SOE-PCR joined the three fragments (using oligos 5673/5676) and the product was cloned into pRB1208 with NheI/BspEI. The pmCherry-EFG1-PrLD plasmid (pRB1224) was constructed by PCR fusion of the N-PrLD region of *EFG1* (PCR amplified from pRB514 with oligos 5578/5579), mCherry (amplified from pRB1207 using oligos 5580/5581) and the C-terminal PrLD of *EFG1* (amplified from pRB514 using oligos 5578/5584). The three fragments were joined by SOE-PCR using oligos 5578/5584 and the resulting product cloned into pRB1207 with NheI/BspEI. The pmCherry-CZF1PrLD plasmid (pRB1218) was constructed by PCR amplifying the CZF1 PrLD region from pRB516 using oligos 5575/5577 and cloned into pRB1207 with BsrGI/BspEI.

C. albicans strain construction. Plasmids containing pMAL2-driven ORFs were linearized using a unique AflII site in the *MAL2* promoter for targeting to the endogenous *MAL2* locus, and transformed using the lithium acetate/PEG/heatshock method. Integration of *pMAL2-WOR1* (pRB488) into a *wor1Δ/Δ* strain (CAY189) to create strains CAY7593/CAY7594 was confirmed by PCR with oligos 317/3727, *pMAL2-WOR1ΔC* (pRB760) was transformed into a *wor1Δ/Δ* strain (CAY189) to create strains CAY8507/CAY8508 and checked by PCR with oligos 3727/3946, *pMAL2-CZF1* (pRB652) was transformed into a *czf1Δ/Δ* strain (CAY191) to create strains CAY7956/CAY7957 and checked by PCR with oligos 3727/3722, and *pMAL2-CZF1ΔN* (pRB653) was transformed into CAY191 to create strains CAY7958/CAY7959 and checked by PCR with oligos 3727/4011. Integration of *pMAL2-WOR4* (pRB755) to create CAY8502, *pMAL2-WOR4ΔN* (pRB757) to create CAY8503/CAY8504, *pMAL2-WOR4ΔC* (pRB758) to create CAY8505/CAY8506 and *pMAL2-WOR4ΔNC* (pRB770) to create CAY8557/CAY8558 was conducted in a *wor4Δ/Δ* strain background (CAY7409) and all were checked by PCR using oligos 3727/3905.

Plasmids with *pMET3*-driven ORFs were linearized using a unique AflII site in the *MET3* promoter and integrated into the *MET3* locus in strain RBY1177 (*MTLα/a*) and integration PCR checked using oligos 317/6007 or 1063/377. The *pMET3-CaWOR1*-GFP strains (CAY11704/CAY11705) used pRB1305, *pMET3-CaWOR1DBD/CmWOR1*PrLD-GFP strains (CAY11706/CAY11707) used pRB1307, *pMET3-CaWOR1DBD/CmWOR1*PrLDΔ260 strains (CAY11736/CAY11737) used pRB1443, *pMET3-CaWOR1DBD/CmWOR1*PrLD(KR-to-G)-GFP strains (CAY11776/CAY11777) used pRB1489, *pMET3-CaWOR1DBD/CmWOR1*PrLD(ΔpolyNQ)-GFP strains (CAY11778/CAY11779) used pRB1491, *pMET3-CaWOR1DBD/CmWOR1*PrLD(YF-to-S)-GFP strains (CAY11780/CAY11781) used pRB1493, *pMET3-CaWOR1DBD/CmWOR1*PrLD(DE-to-A)-GFP strains (CAY11712/CAY11713) used pRB1425, *pMET3-CaWOR1DBD/TAF15*PrLD strains (CAY11772/CAY11773) used pRB1485 and *pMET3-CaWOR1DBD/CaCZF1*PrLD strains (CAY11774/CAY11775) used pRB1485.

White–opaque cell determination assays. For *pMAL2*-driven constructs, cells in the white phenotypical state were cultured overnight in liquid YPD medium at 30 °C. Cells per millilitre were estimated using optical density with $1 OD_{600} = 2 \times 10^7$ cells ml⁻¹ (where OD_{600} is the absorbance or optical density at 600 nm). Cultures were serially diluted in phosphate-buffered saline (PBS) to 2×10^3 cells ml⁻¹ and approximately 100 cells were spread plated in duplicate on synthetic complete dextrose (SCD) and SC maltose media. Plates were incubated at 22 °C for 7 d, and the colonies were counted and scored for the presence of opaque sectors. For *pMET3*-driven constructs, white state cells were grown on synthetic dropout medium containing 5 mM methionine and cysteine (SD + Met)⁷³, suspended in PBS, serially diluted, and then plated on synthetic dropout medium lacking these amino acids (SD – Met) and SD + Met, and incubated at 22 °C for 7 d before scoring for the presence of opaque colonies and sectors.

Candida cell imaging. Cells were grown for 2 d on SD + Met and then used to inoculate 3-mL cultures in SD – Met and SD + Met, which were then incubated at 22 °C for 18 h; 200 µL of each culture was diluted 1:5 in fresh medium and 10 µL of 1 mg ml⁻¹ of Hoechst 33258 was added. After 20 min with shaking, cells were pelleted and resuspended in 100 µL of fresh medium. Cells were imaged using a Zeiss Axio Observer Z1 inverted fluorescence microscope for fluorescence and DIC imaging equipped with Zen software (Zen v.3.0 blue edition).

Protein purification. His-MBP fusion protein constructs were transformed into BL21 (DE3) Star *E. coli* cells for expression. Cells were grown at 37 °C overnight, then diluted 1:100 into fresh Luria broth (LB) medium, cultured at 37 °C until they reached an OD_{600} of 0.5–0.7, and then induced with 1 mM isopropyl β-D-1-thiogalactopyranoside. Induction conditions for most MBP-fusion proteins were 30 °C for 4 h, with the exception of MBP-Wor1 (30 °C, 8 h), MBP-Efg1

(25 °C, overnight), MBP-Wor4 (18 °C, 8 h), MBP-Efg1[N-GFP-C] (25 °C, 4 h) and MBP-Wor1[GFP-C] (25 °C, 4 h). For most purified proteins, cells were lysed with lysozyme followed by sonication in lysis buffer consisting of 10 mM Tris, pH 7.4, 1 M NaCl, 1 mM phenylmethylsulfonyl fluoride and a protease inhibitor cocktail (Thermo Scientific Pierce Protease Inhibitor). For purification of MBP-Czf1, MBP-Czf1ΔN, MBP-Efg1ΔN, MBP-Efg1ΔC, MBP-Wor4ΔN, MBP-Wor4ΔC, MBP-Wor4ΔNC and MBP-GFP, cells were lysed for 30 min at 22 °C using 4 mL Bacterial Protein Extraction Reagent (Thermo Fisher Scientific; supplemented with 1 M NaCl) per gram of *E. coli* pellet wet weight. Proteins were purified by nickel affinity chromatography, followed by size exclusion using a Sephadryl S300 26/60 column (GE Healthcare). Fractions were concentrated using Amicon Ultra 50K concentrators (Millipore) and snap frozen in liquid nitrogen. The MBP-CaWor1-DBD/CmWor1-PrLD protein was concentrated using a Pierce PES concentrator (Thermo Fisher Scientific).

PLAAC analysis. Protein sequences were analysed by PLAAC (<http://plaac.wi.mit.edu>)⁴¹.

Phase separation assays. Protein stocks were thawed at 22 °C and diluted in 10 mM Tris-HCl, pH 7.4, 150 mM NaCl. Aliquots were further concentrated in centrifugal filter units (Amicon Ultra—0.5-ml centrifugal filter units) to a volume of 100 µL. Protein concentration was measured with a Nanodrop 2000c (Thermo Fisher Scientific) and diluted in 10 mM Tris-HCl buffer with 150 mM NaCl to appropriate concentrations, as indicated for each assay. Protein reactions with TEV were set up in 10-µL total volumes (9.5 µL protein with 0.5 µL of 0.3 mg ml⁻¹ of TEV) and incubated for 30 min at 22 °C. Where noted, 5% PEG-8000 was also included in the reactions. Fluorescent labelling of proteins with DyLight fluorophore dyes (Thermo Fisher Scientific, DyLight NHS Esters 405, 488, 550, 633) was carried out per the manufacturer's instructions after buffer exchange into 10 mM sodium phosphate buffer, pH 7.5, 150 mM NaCl using Amicon Ultra 0.5 filter units. Labelled proteins were added to assays at indicated concentrations before TEV incubation. For DNA phase separation assays, λ phage DNA (Thermo Fisher Scientific) or *C. albicans* SC5314 gDNA was diluted in 10 mM Tris-HCl, pH 7.4, 150 mM NaCl, and added to indicated proteins at a final concentration of 9.4 nM or 50 nM, respectively, before TEV incubation. Proteins were imaged immediately after incubation on chamber slides (Polysciences, 10-chamber slides), with 2.5 µL solution per chamber, sealed using a glass coverslip. All images were acquired at $\times 63$ initial magnification with a Zeiss Axio Observer Z1 inverted fluorescence microscope for fluorescence and DIC imaging, or at $\times 60$ initial magnification with an Olympus FV3000 Confocal Microscope. The Zeiss microscope was equipped with AxioVision software (v.4.8) and Zen software (v.3.0 blue edition), and the Olympus microscope was equipped with CellSens software (v.1.17). For time-lapse imaging of droplet fusion events, proteins were imaged under DIC or the appropriate channel for each DyLight dye detailed above at the indicated conditions, and images acquired every second (Efg1 and Efg1 bulk with DyLight-labelled proteins) or every 10 s (Czf1). Post-imaging processing was carried out in FIJI (ImageJ v.1.52p).

Hexanediol treatment of TF condensates. Protein stocks were prepared as detailed in 'Phase separation assays', and digested with TEV before the addition of hexanediol. After TEV incubation, proteins were treated with 1,6-hexanediol (Sigma-Aldrich) or 2,5-hexanediol (Thermo Fisher Scientific) at 10% m:v concentrations in 10 mM Tris-HCl, pH 7.4, 150 mM NaCl. Hexanediol medium was added to proteins in buffer, mixed well by pipetting up and down, and allowed to incubate at 22 °C for 10 min. Proteins were then immediately imaged as described in 'Phase separation assays'. For Wor4, where noted, hexanediol was added to the protein stock before the addition of 5% PEG-8000 and TEV. The protein was incubated with hexanediol for 10 min at 22 °C, after which time PEG and TEV were added and an additional 30-min incubation was carried out. The protein condensates were then immediately imaged. All images were acquired at $\times 63$ initial magnification with a Zeiss Axio Observer Z1 inverted fluorescence microscope equipped with AxioVision software (v.4.8) and Zen software (v.3.0 blue edition).

Partitioning of GFP-PrLD protein constructs into Efg1 droplets. GFP-PrLD fusion proteins were concentrated in 10 mM Tris-HCl, pH 7.4, 150 mM NaCl, and then diluted in this buffer to 30 µM. Efg1 was present at a 30 µM concentration in each assay, with the GFP-PrLD proteins added at a 1:10 dilution for a final concentration of 3 µM. Proteins were incubated at 22 °C for 30 min in 10-µL volumes and then imaged immediately in chamber slides. Images were acquired at $\times 63$ initial magnification with a Zeiss Axio Observer Z1 inverted fluorescence microscope equipped with AxioVision software (v.4.8). Fluorescent signals were calculated with FIJI (ImageJ v.1.52p). To calculate enrichment ratios, mean fluorescence intensity signal per unit area inside each Efg1 condensate was divided by the mean fluorescence intensity signal per unit area outside each condensate (after subtracting background fluorescence signal). Background fluorescence was calculated with FIJI for images of Efg1 condensates without the presence of GFP-PrLD protein constructs.

Mammalian cell culture, live-cell imaging and LacO array analysis. Human U2OS cells containing a LacO array (~50,000 LacO elements) were a gift from the Tjian Lab⁵⁰. U2OS cells were grown in low-glucose Dulbecco's modified Eagle's medium (DMEM, Thermo Fisher Scientific) supplemented with 10% fetal bovine serum (Thermo Fisher Scientific) and 1% penicillin–streptomycin (Thermo Fisher Scientific), and cultured at 37 °C with 5% CO₂. For live-cell imaging, cells were plated in 24-well, glass-bottomed dishes (Cellvis), then transfected with the desired plasmid construct(s) using Lipofectamine 3000 (Thermo Fisher Scientific) and grown for 24 h. The medium was changed to fresh DMEM and cells imaged with a Zeiss Axio Observer Z1 inverted fluorescence microscope for fluorescence (EYFP and mCherry) and DIC imaging at ×40 magnification. The microscope was equipped with AxioVision software (v.4.8) and Zen software (v.3.0 blue edition). Post-imaging processing was carried out in FIJI (ImageJ v.1.52p).

For quantification of the Lacl–EYFP–PrLD constructs bound at the LacO array, a perimeter was drawn around each array spot in FIJI and then analysed through the measurement tool for both array area and maximum fluorescence intensity. Background fluorescence intensity was corrected for by subtracting fluorescence signal immediately outside the array spot in the cell nucleus. To quantify mCherry–PrLD enrichment at the LacO array bound by PrLD–Lacl–EYFP constructs, we followed a method similar to that employed by Chong et al.⁸. Briefly, the array spot was measured in the EYFP channel to determine array location, then the mCherry channel measured for maximum fluorescence intensity at the array (I_{peak}). Two locations immediately adjacent to the array in the mCherry channel were then measured and averaged ($I_{\text{periphery}}$) to represent average background fluorescent signal in the cell nucleus. The mCherry–PrLD enrichment at the LacO array was then calculated as the ratio of the peak signal divided by the background signal ($I_{\text{peak}}/I_{\text{periphery}}$). When the ratio is >1 it is indicative of PrLD–PrLD-mediated interactions.

Hexanediol treatment of PrLD-mediated LacO array cellular condensates.

U2OS cells containing the LacO array and transfected with Lacl–EYFP–PrLD constructs were treated with 1,6-hexanediol (Sigma-Aldrich) or 2,5-hexanediol (Thermo Fisher Scientific). These compounds were prepared in fresh, pre-warmed DMEM at 20% m:v concentrations. U2OS cells were placed in 1 ml fresh DMEM in a 24-well, glass-bottomed dish, so that addition of 1 ml hexanediol medium yielded a final concentration of 10% 1,6- or 2,5-hexanediol. Images were taken directly before addition of the hexanediol medium and then immediately after for a total of 7 min, with images acquired every 10 s using a Zeiss Axio Observer Z1 microscope for fluorescence (EYFP) and DIC imaging at ×40 magnification. The microscope was equipped with AxioVision software (v.4.8) and Zen software (v.3.0 blue edition). Time point $t=0$ corresponds to cells directly before hexanediol addition, whereas $t=30$ corresponds to cells 30 s after addition of the medium. Intranuclear condensates not associated with the LacO array were quantified by counting puncta in FIJI (ImageJ v.1.52p).

Single-molecule experiments and analysis.

Microscope slides were microfabricated and assembled into flowcells as described previously^{50,74}. Single-molecule images were collected with a Nikon Ti-E inverted microscope customized with a prism-TIRF configuration. Flowcells were illuminated by a 488-nm laser (Coherent). Laser power was 40 mW at the front face of the prism. Fluorescent images were collected by two EM-CCD cameras (Andor iXon DU897, –80 °C) using a 638-nm dichroic beam splitter (Chroma). Nikon NIS-Elements software (v.4.30.02) was used to collect the single-molecule data at a frame rate of 250 ms. All images were saved as TIFF files without compression for further image analysis in ImageJ (v.1.52p).

DNA substrates for single-molecule imaging. The cohesive ends of bacteriophage λ DNA (New England Biolabs) were ligated to oligonucleotides IF003 and IF004 to label DNA with biotin and digoxigenin (Dig), respectively⁵². After ligation, the DNA substrate was separated from the oligonucleotides and T4 DNA ligase via gel filtration on an S-1000 column (GE Healthcare). Where indicated, nucleosomes were deposited onto this DNA substrate⁵¹. For nucleosome reconstitution, the DNA substrate was mixed with sodium acetate, pH 5.5, to 0.3 M and isopropanol to 1:1 (v:v), then precipitated by centrifugation at 15,000g for 30 min. The invisible DNA precipitate was washed with 70% ethanol and dissolved in 2 M TE buffer (10 mM Tris-HCl, pH 8.0, 1 mM ethylenediaminetetraacetic acid (EDTA), 2 M NaCl) to obtain concentrated DNA at ~150 ng μl⁻¹. For reconstitution, 0.8 nM of the DNA was prepared in 2 M TE buffer with 1 mM dithiothreitol (DTT) for a total volume of 100 μl. Human histone octamers containing 3× HA-labelled H2A with wild-type H2B, H3 and H4 were added to the DNA. The mixture was dialysed using a mini-dialysis button (10-kDa molecular mass cutoff, Bio-Rad) against 400 ml dialysis buffer (10 mM Tris-HCl, pH 7.6, 1 mM EDTA, 1 mM DTT, and gradually decreasing concentration of NaCl). The salt gradient dialysis was started with 1.5 M NaCl at 4 °C. Dialysis buffer was exchanged every 2 h to decrease salt concentrations from 1 M to 0.2 M in 0.2-M steps. The last 0.2 M NaCl buffer was used for overnight dialysis.

Imaging DNA condensation by TFs. All single-molecule experiments were conducted in imaging buffer (40 mM Tris-HCl, pH 8.0, 1 mM MgCl₂, 0.2 mg ml⁻¹ of

bovine serum albumin, 50 mM NaCl, 1 mM DTT). DNA contraction was observed via a fluorescent signal on the diglycated DNA ends. These ends were fluorescently labelled by injecting 100 μl of 10 nM anti-Dig antibodies (Life Technologies, catalogue no. 9H27L19) and 700 μl of 2 nM α-rabbit antibody-conjugated quantum dots (Life Technologies, catalogue no. Q-11461MP) into the flowcell. After labelling Dig-ends of DNA, the single-tethered DNA molecules were elongated by consistently applying a flow rate of 450 μl min⁻¹. For TF-driven DNA condensation, unless otherwise stated, 10–300 nM of the indicated TF was incubated with 100 μg μl⁻¹ of TEV protease in 1 ml imaging buffer for 5 min at 22 °C, then injected into the flowcell at a flow rate of 450 μl min⁻¹. The position of quantum dot-labelled DNA ends was recorded for up to 20 min. Nucleosomes were labelled using a rabbit α-HA antibody (ICL, catalogue no. RHGT-45A-Z) against the 3× HA epitope on histone H2A, followed by binding of an Alexa-488-conjugated α-rabbit antibody (Thermo Fisher Scientific, catalogue no. A-11008).

Observing TF recruitment via the prion-like domains. Double-tethered DNA curtains were used to determine whether TFs can interact via their PrLDs. In this assay, the DNA is captured and extended between a chromium barrier and an α-Dig antibody deposited on a chromium pedestal⁷⁴. Keeping the DNA fully extended prevents TF-driven compaction. Next, 300 nM 6x His-MBP-Efg1 was first injected without TEV cleavage, then 300 nM GFP-Efg1ΔDBD or GFP-Wor1ΔDBD incubated with 100 μg μl⁻¹ of TEV for 5 min was injected on to the Efg1-coated DNA molecules.

Particle tracking and data analysis. Fluorescently labelled DNA ends were tracked in ImageJ with a customized particle-tracking script and the resulting trajectories were further analysed in MATLAB (R2015a, MathWorks). The time-dependent positions of DNA ends were determined by fitting a single fluorescent particle to a two-dimensional Gaussian distribution, and the series of sub-pixel positions was generated for each trajectory. We conducted a two-sample, one-sided Kolmogorov–Smirnov test to determine whether distributions of length or rate of DNA condensation differ, based on protein concentration and the presence of nucleosomes or TEV protease using the PAST3 software package (v.3.24)⁷⁵.

Statistical analysis. Statistical methods were not used to predetermine sample sizes for any experiments throughout the present study. No randomization or blinding was carried out during either the experiments or the analysis of results. At least ten images were taken for all microscopy imaging involving purified proteins and live cells, except for images acquired for full-length Efg1 with GFP-fusion proteins, in which at least five images were taken. Each experiment was repeated at least twice to demonstrate reproducibility. Sample sizes were sufficient based on differences between different experimental groups, with $P<0.05$ detected.

All quantitative data shown in this study for bar graphs represent the mean ± s.d. Bar plots have been overlaid with individual data points whenever possible. Quantitative data for box-and-whisker plots represent all data points, maximum to minimum, with the central line corresponding to the median, the '+' corresponding to the mean, the 25th to 75th percentiles corresponding to the box and the 95th to 5th percentiles corresponding to the whiskers. Data presented in box plots show the median (central line) and 10th to 90th percentiles (ends of box). Individual data points are overlaid on the plots.

All data points were recorded and taken into account for analysis to accurately represent biological and technical replicates for each experiment performed. Statistical analysis was carried out using GraphPad Prism software (v.8.4.2). Calculations for statistical significance were performed using the following tests: two-tailed, unpaired Mann–Whitney U-test; two-sample, one-sided Kolmogorov–Smirnov test; ordinary one-way analysis of variance (ANOVA) with Dunnett's multiple-comparison test; and two-tailed, unpaired Student's *t*-test with Welch's correction. Experiments were repeated at least twice unless otherwise noted, and were reproducible throughout.

Reporting summary. Further information on research design is available in the Nature Research Reporting Summary linked to this article.

Data availability

Data that support the findings of this study are available from the corresponding author upon request. Source data are provided with this paper.

Received: 4 December 2019; Accepted: 25 June 2020;
Published online: 27 July 2020

References

- Wilkinson, A. C., Nakauchi, H. & Gottgens, B. Mammalian transcription factor networks: recent advances in interrogating biological complexity. *Cell Syst.* **5**, 319–331 (2017).
- Moris, N., Pina, C. & Arias, A. M. Transition states and cell fate decisions in epigenetic landscapes. *Nat. Rev. Genet.* **17**, 693–703 (2016).
- Sabari, B. R. et al. Coactivator condensation at super-enhancers links phase separation and gene control. *Science* **361**, eaar3958 (2018).

4. Plys, A. J. & Kingston, R. E. Dynamic condensates activate transcription. *Science* **361**, 329–330 (2018).
5. Patel, A. et al. A liquid-to-solid phase transition of the ALS protein FUS accelerated by disease mutation. *Cell* **162**, 1066–1077 (2015).
6. Kato, M. et al. Cell-free formation of RNA granules: low complexity sequence domains form dynamic fibers within hydrogels. *Cell* **149**, 753–767 (2012).
7. Burke, K. A., Janke, A. M., Rhine, C. L. & Fawzi, N. L. Residue-by-residue view of in vitro FUS granules that bind the C-terminal domain of RNA polymerase II. *Mol. Cell* **60**, 231–241 (2015).
8. Chong, S. et al. Imaging dynamic and selective low-complexity domain interactions that control gene transcription. *Science* **361**, eaar2555 (2018).
9. Hnisz, D., Shrinivas, K., Young, R. A., Chakraborty, A. K. & Sharp, P. A. A phase separation model for transcriptional control. *Cell* **169**, 13–23 (2017).
10. Nair, S. J. et al. Phase separation of ligand-activated enhancers licenses cooperative chromosomal enhancer assembly. *Nat. Struct. Mol. Biol.* **26**, 193–203 (2019).
11. Hnisz, D. et al. Super-enhancers in the control of cell identity and disease. *Cell* **155**, 934–947 (2013).
12. Mansour, M. R. et al. An oncogenic super-enhancer formed through somatic mutation of a noncoding intergenic element. *Science* **346**, 1373–1377 (2014).
13. Pott, S. & Lieb, J. D. What are super-enhancers? *Nat. Genet.* **47**, 8–12 (2015).
14. Whyte, W. A. et al. Master transcription factors and mediator establish super-enhancers at key cell identity genes. *Cell* **153**, 307–319 (2013).
15. Parker, S. C. et al. Chromatin stretch enhancer states drive cell-specific gene regulation and harbor human disease risk variants. *Proc. Natl Acad. Sci. USA* **110**, 17921–17926 (2013).
16. Niederriter, A. R., Varshney, A., Parker, S. C. & Martin, D. M. Super enhancers in cancers, complex disease, and developmental disorders. *Genes* **6**, 1183–1200 (2015).
17. Loven, J. et al. Selective inhibition of tumor oncogenes by disruption of super-enhancers. *Cell* **153**, 320–334 (2013).
18. Varshney, A. et al. Cell specificity of human regulatory annotations and their genetic effects on gene expression. *Genetics* **211**, 549–562 (2018).
19. Deitsch, K. W., Lukehart, S. A. & Stringer, J. R. Common strategies for antigenic variation by bacterial, fungal and protozoan pathogens. *Nat. Rev. Microbiol.* **7**, 493–503 (2009).
20. Noble, S. M., Gianetti, B. A. & Witchley, J. N. *Candida albicans* cell-type switching and functional plasticity in the mammalian host. *Nat. Rev. Microbiol.* **15**, 96–108 (2017).
21. Norman, T. M., Lord, N. D., Paulsson, J. & Losick, R. Stochastic switching of cell fate in microbes. *Annu. Rev. Microbiol.* **69**, 381–403 (2015).
22. Ackermann, M. A functional perspective on phenotypic heterogeneity in microorganisms. *Nat. Rev. Microbiol.* **13**, 497–508 (2015).
23. Slutsky, B. et al. ‘White–opaque transition’: a second high-frequency switching system in *Candida albicans*. *J. Bacteriol.* **169**, 189–197 (1987).
24. Kvaal, C. et al. Misexpression of the opaque-phase-specific gene *PEP1* (*SAP1*) in the white phase of *Candida albicans* confers increased virulence in a mouse model of cutaneous infection. *Infect. Immun.* **67**, 6652–6662 (1999).
25. Kvaal, C. A., Srikantha, T. & Soll, D. R. Misexpression of the white-phase-specific gene *WH11* in the opaque phase of *Candida albicans* affects switching and virulence. *Infect. Immun.* **65**, 4468–4475 (1997).
26. Mallick, E. M. et al. Phenotypic plasticity regulates *Candida albicans* interactions and virulence in the vertebrate host. *Front. Microbiol.* **7**, 780 (2016).
27. Hernday, A. D. et al. Structure of the transcriptional network controlling white–opaque switching in *Candida albicans*. *Mol. Microbiol.* **90**, 22–35 (2013).
28. Hernday, A. D. et al. *Ssn6* defines a new level of regulation of white–opaque switching in *Candida albicans* and is required for the stochasticity of the switch. *mBio* **7**, e01565–15 (2016).
29. Huang, G. et al. Bistable expression of *WOR1*, a master regulator of white–opaque switching in *Candida albicans*. *Proc. Natl Acad. Sci. USA* **103**, 12813–12818 (2006).
30. Lohse, M. B. et al. Identification and characterization of a previously undescribed family of sequence-specific DNA-binding domains. *Proc. Natl Acad. Sci. USA* **110**, 7660–7665 (2013).
31. Lohse, M. B. & Johnson, A. D. Identification and characterization of *Wor4*, a new transcriptional regulator of white–opaque switching. *G3 (Bethesda)* **6**, 721–729 (2016).
32. Srikantha, T. et al. *TOS9* regulates white–opaque switching in *Candida albicans*. *Eukaryot. Cell* **5**, 1674–1687 (2006).
33. Srikantha, T., Tsai, L. K., Daniels, K. & Soll, D. R. *EFG1* null mutants of *Candida albicans* switch but cannot express the complete phenotype of white-phase budding cells. *J. Bacteriol.* **182**, 1580–1591 (2000).
34. Wang, H. et al. *Candida albicans* Zef37, a zinc finger protein, is required for stabilization of the white state. *FEBS Lett.* **585**, 797–802 (2011).
35. Zordan, R. E., Galgoczy, D. J. & Johnson, A. D. Epigenetic properties of white–opaque switching in *Candida albicans* are based on a self-sustaining transcriptional feedback loop. *Proc. Natl Acad. Sci. USA* **103**, 12807–12812 (2006).
36. Zordan, R. E., Miller, M. G., Galgoczy, D. J., Tuch, B. B. & Johnson, A. D. Interlocking transcriptional feedback loops control white–opaque switching in *Candida albicans*. *PLoS Biol.* **5**, e256 (2007).
37. Frazer, C., Hernday, A. D. & Bennett, R. J. Monitoring phenotypic switching in *Candida albicans* and the use of next-gen fluorescence reporters. *Curr. Protoc. Microbiol.* **53**, e76 (2019).
38. Morrow, B., Srikantha, T., Anderson, J. & Soll, D. R. Coordinate regulation of two opaque-phase-specific genes during white–opaque switching in *Candida albicans*. *Infect. Immun.* **61**, 1823–1828 (1993).
39. Srikantha, T. & Soll, D. R. A white-specific gene in the white–opaque switching system of *Candida albicans*. *Gene* **131**, 53–60 (1993).
40. Jenull, S. et al. The *Candida albicans* HIR histone chaperone regulates the yeast-to-hyphae transition by controlling the sensitivity to morphogenesis signals. *Sci. Rep.* **7**, 8308 (2017).
41. Lancaster, A. K., Nutter-Upham, A., Lindquist, S. & King, O. D. PLAAC: a web and command-line application to identify proteins with prion-like amino acid composition. *Bioinformatics* **30**, 2501–2502 (2014).
42. Franzmann, T. & Alberti, S. Prion-like low-complexity sequences: key regulators of protein solubility and phase behavior. *J. Biol. Chem.* **294**, 7128–7136 (2018).
43. Wang, J. et al. A molecular grammar governing the driving forces for phase separation of prion-like RNA binding proteins. *Cell* **174**, 688–699 (2018).
44. Ribbeck, K. & Gorlich, D. The permeability barrier of nuclear pore complexes appears to operate via hydrophobic exclusion. *EMBO J.* **21**, 2664–2671 (2002).
45. Kroschwitz, S., Maharanan, S. & Simon, A. Hexanediol: a chemical probe to investigate the material properties of membrane-less compartments. *Matters* **3**, e201702000010 (2017).
46. Kato, M. & McKnight, S. L. A solid-state conceptualization of information transfer from gene to message to protein. *Annu. Rev. Biochem.* **87**, 351–390 (2018).
47. Doedt, T. et al. APSES proteins regulate morphogenesis and metabolism in *Candida albicans*. *Mol. Biol. Cell* **15**, 3167–3180 (2004).
48. Zhao, Y. et al. The APSES family proteins in fungi: characterizations, evolution and functions. *Fungal Genet. Biol.* **81**, 271–280 (2015).
49. Larson, A. G. et al. Liquid droplet formation by HP1α suggests a role for phase separation in heterochromatin. *Nature* **547**, 236–240 (2017).
50. Soniat, M. M. et al. Next-generation DNA curtains for single-molecule studies of homologous recombination. *Methods Enzymol.* **592**, 259–281 (2017).
51. Brown, M. W. et al. Dynamic DNA binding licenses a repair factor to bypass roadblocks in search of DNA lesions. *Nat. Commun.* **7**, 10607 (2016).
52. Myler, L. R. et al. Single-molecule imaging reveals the mechanism of Exo1 regulation by single-stranded DNA binding proteins. *Proc. Natl Acad. Sci. USA* **113**, E1170–E1179 (2016).
53. Hyman, A. A., Weber, C. A. & Julicher, F. Liquid–liquid phase separation in biology. *Annu. Rev. Cell Dev. Biol.* **30**, 39–58 (2014).
54. Greig, J. A. et al. Arginine-enriched mixed-charge domains provide cohesion for nuclear speckle condensation. *Mol. Cell* **77**, 1237–1250 (2020).
55. Nott, T. J. et al. Phase transition of a disordered nuage protein generates environmentally responsive membraneless organelles. *Mol. Cell* **57**, 936–947 (2015).
56. Pak, C. W. et al. Sequence determinants of intracellular phase separation by complex coacervation of a disordered protein. *Mol. Cell* **63**, 72–85 (2016).
57. Murthy, A. C. et al. Molecular interactions underlying liquid–liquid phase separation of the FUS low-complexity domain. *Nat. Struct. Mol. Biol.* **26**, 637–648 (2019).
58. Boija, A. et al. Transcription factors activate genes through the phase-separation capacity of their activation domains. *Cell* **175**, 1842–1855 (2018).
59. Janicki, S. M. et al. From silencing to gene expression: real-time analysis in single cells. *Cell* **116**, 683–698 (2004).
60. Owen, I. & Shewmaker, F. The role of post-translational modifications in the phase transitions of intrinsically disordered proteins. *Int. J. Mol. Sci.* **20**, 5501 (2019).
61. Alby, K. & Bennett, R. J. Stress-induced phenotypic switching in *Candida albicans*. *Mol. Biol. Cell* **20**, 3178–3191 (2009).
62. Shrinivas, K. et al. Enhancer features that drive formation of transcriptional condensates. *Mol. Cell* **75**, 549–561 (2019).
63. Boehning, M. et al. RNA polymerase II clustering through carboxy-terminal domain phase separation. *Nat. Struct. Mol. Biol.* **25**, 833–840 (2018).
64. Kwon, I. et al. Phosphorylation-regulated binding of RNA polymerase II to fibrous polymers of low-complexity domains. *Cell* **155**, 1049–1060 (2013).
65. McSwiggen, D. T., Mir, M., Darzacq, X. & Tjian, R. Evaluating phase separation in live cells: diagnosis, caveats, and functional consequences. *Genes Dev.* **33**, 1619–1634 (2019).
66. Nobile, C. J. et al. A recently evolved transcriptional network controls biofilm development in *Candida albicans*. *Cell* **148**, 126–138 (2012).
67. Fox, E. P. et al. An expanded regulatory network temporally controls *Candida albicans* biofilm formation. *Mol. Microbiol.* **96**, 1226–1239 (2015).
68. Homann, O. R. & Johnson, A. D. MochiView: versatile software for genome browsing and DNA motif analysis. *BMC Biol.* **8**, 49 (2010).

69. Peti, W. & Page, R. Strategies to maximize heterologous protein expression in *Escherichia coli* with minimal cost. *Protein Expr. Purif.* **51**, 1–10 (2007).
70. Horton, R. M., Hunt, H. D., Ho, S. N., Pullen, J. K. & Pease, L. R. Engineering hybrid genes without the use of restriction enzymes: gene splicing by overlap extension. *Gene* **77**, 61–68 (1989).
71. Reuss, O., Vik, A., Kolter, R. & Morschhauser, J. The *SAT1* flipper, an optimized tool for gene disruption in *Candida albicans*. *Gene* **341**, 119–127 (2004).
72. Gerami-Nejad, M., Dulmage, K. & Berman, J. Additional cassettes for epitope and fluorescent fusion proteins in *Candida albicans*. *Yeast* **26**, 399–406 (2009).
73. Care, R. S., Trevethick, J., Binley, K. M. & Sudbery, P. E. The *MET3* promoter: a new tool for *Candida albicans* molecular genetics. *Mol. Microbiol.* **34**, 792–798 (1999).
74. Gallardo, I. F. et al. High-throughput universal DNA curtain arrays for single-molecule fluorescence imaging. *Langmuir* **31**, 10310–10317 (2015).
75. Hammer, O., Harper, D. A. & Ryan, P. D. PAST: paleontological statistics software package for education and data analysis. *Palaeontol. Electron.* **4**, 1–9 (2001).

Acknowledgements

We thank R. Tjian for the gift of reporter cell lines, S. Sandler and J. Morschhauser for plasmids, L. Brossay for help with tissue culture, G. Williams for help with confocal microscopy, and members of the Bennett laboratory for helpful discussions. This work is supported by the National Institute of Allergy and Infectious Disease (grant nos. AI081704, AI135228 and AI141893 to R.J.B. and AI137975 to A.D.H.), the Burroughs Wellcome Fund (PATH award to R.J.B.), the National Heart, Lung and Blood Institute (grant no. T32HL134625 to M.I.S.), the National Institute of Dental and Craniofacial Research (grant no. F31DE02968001 to M.I.S.), the National Institute of Mental Health (grant no. T32MH020068 to V.H.R.), the National Institute of Neurological Disorders and Stroke (grant no. F31NS110301 to V.H.R.), a Howard Hughes Medical Institute

International Student Fellowship (to Y.K.), the National Institute of General Medical Sciences (grant nos. GM120554 to I.J.F. and GM118530 to N.L.F.), the Welch Foundation (grant no. F-1808 to I.J.F.) and the National Science Foundation (grant nos. 1453358 to I.J.F. and 1845734 to N.L.F.).

Author contributions

C.F. and R.J.B. conceived the study. C.F., M.I.S., Y.K., M.H., M.A.D., N.V.J., A.D.H., V.H.R. and R.J.B. investigated the study. C.F., M.I.S., Y.K. and A.H. formally analysed the study. N.V.J., A.H., N.L.F., I.J.F. and R.J.B. provided the resources. C.F., M.I.S. and R.J.B. wrote the original draft of the manuscript. C.F., M.I.S., A.D.H., N.L.F., I.J.F. and R.J.B. reviewed and edited the manuscript. C.F., M.I.S., Y.K. and A.D.H. visualized the study. N.L.F., I.J.F. and R.J.B. supervised it. A.D.H., N.L.F., I.J.F. and R.J.B. acquired the funding.

Competing interests

The authors declare no competing interests.

Additional information

Extended data is available for this paper at <https://doi.org/10.1038/s41564-020-0760-7>.

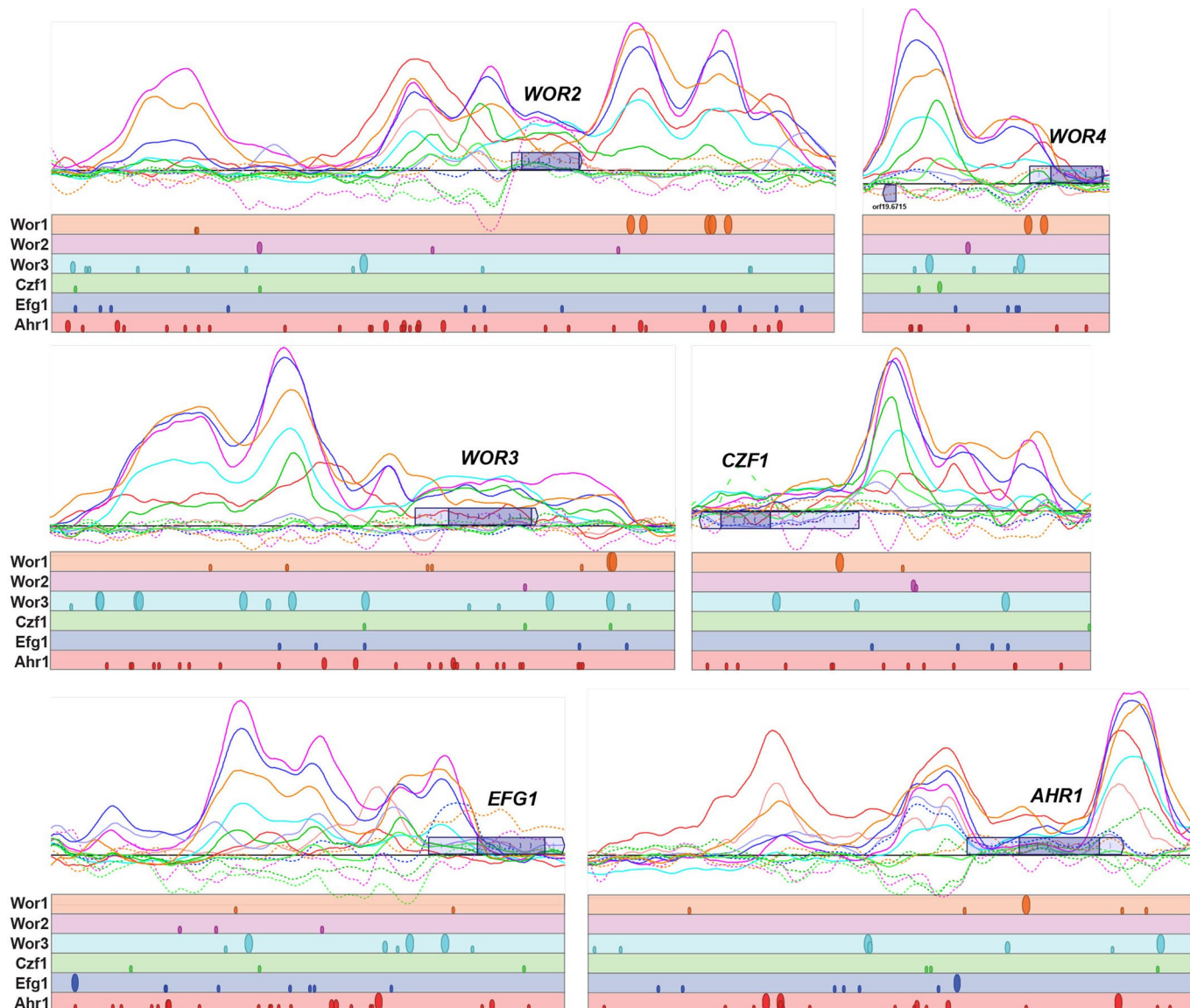
Supplementary information is available for this paper at <https://doi.org/10.1038/s41564-020-0760-7>.

Correspondence and requests for materials should be addressed to R.J.B.

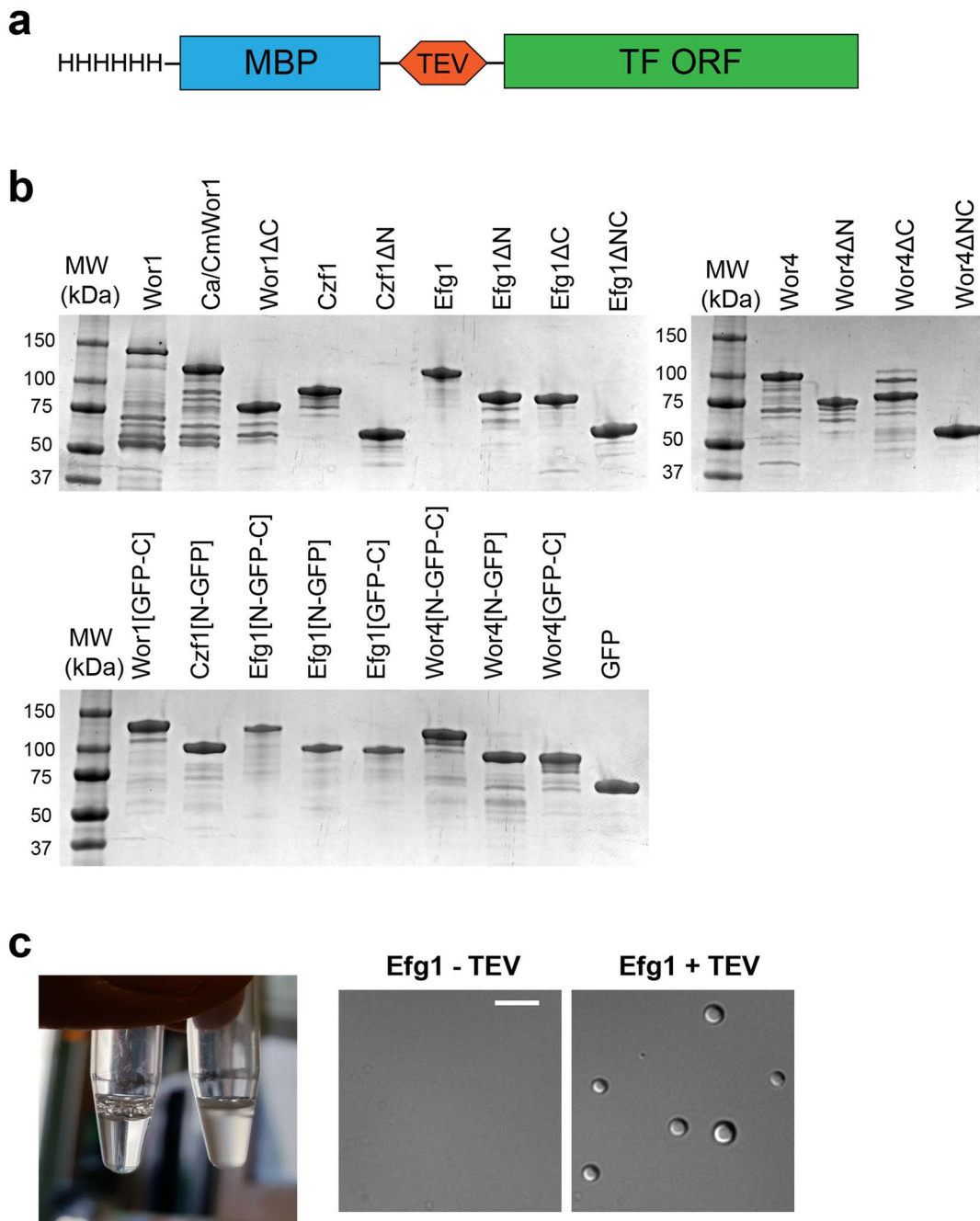
Reprints and permissions information is available at www.nature.com/reprints.

Publisher's note Springer Nature remains neutral with regard to jurisdictional claims in published maps and institutional affiliations.

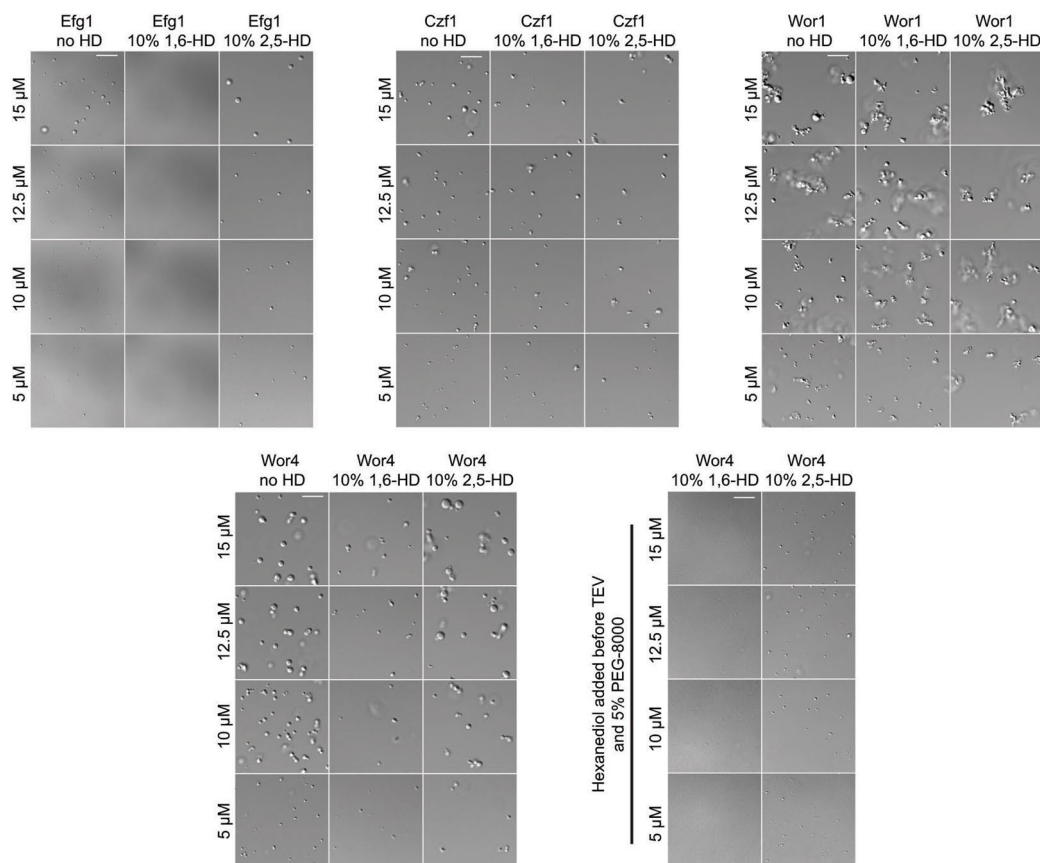
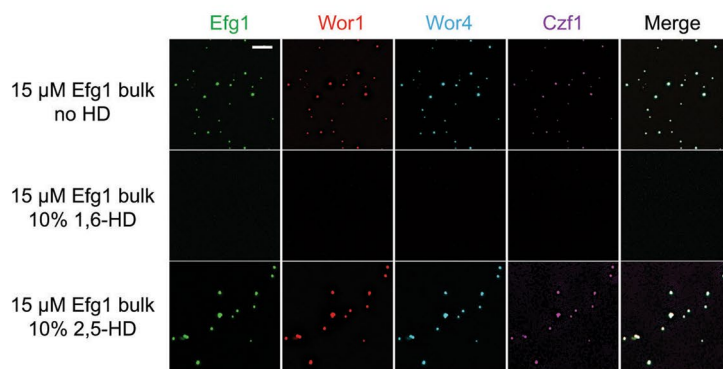
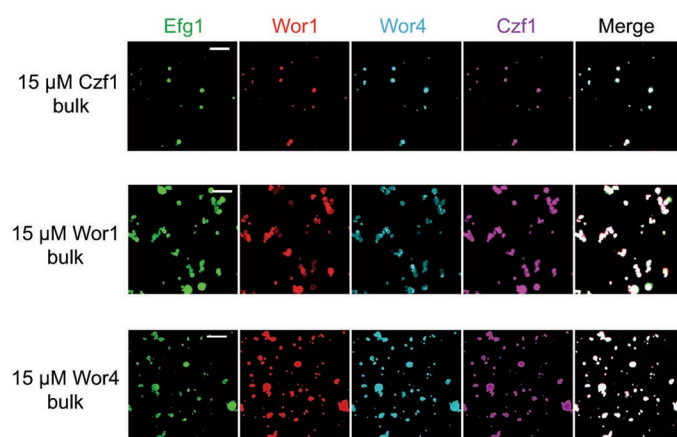
© The Author(s), under exclusive licence to Springer Nature Limited 2020



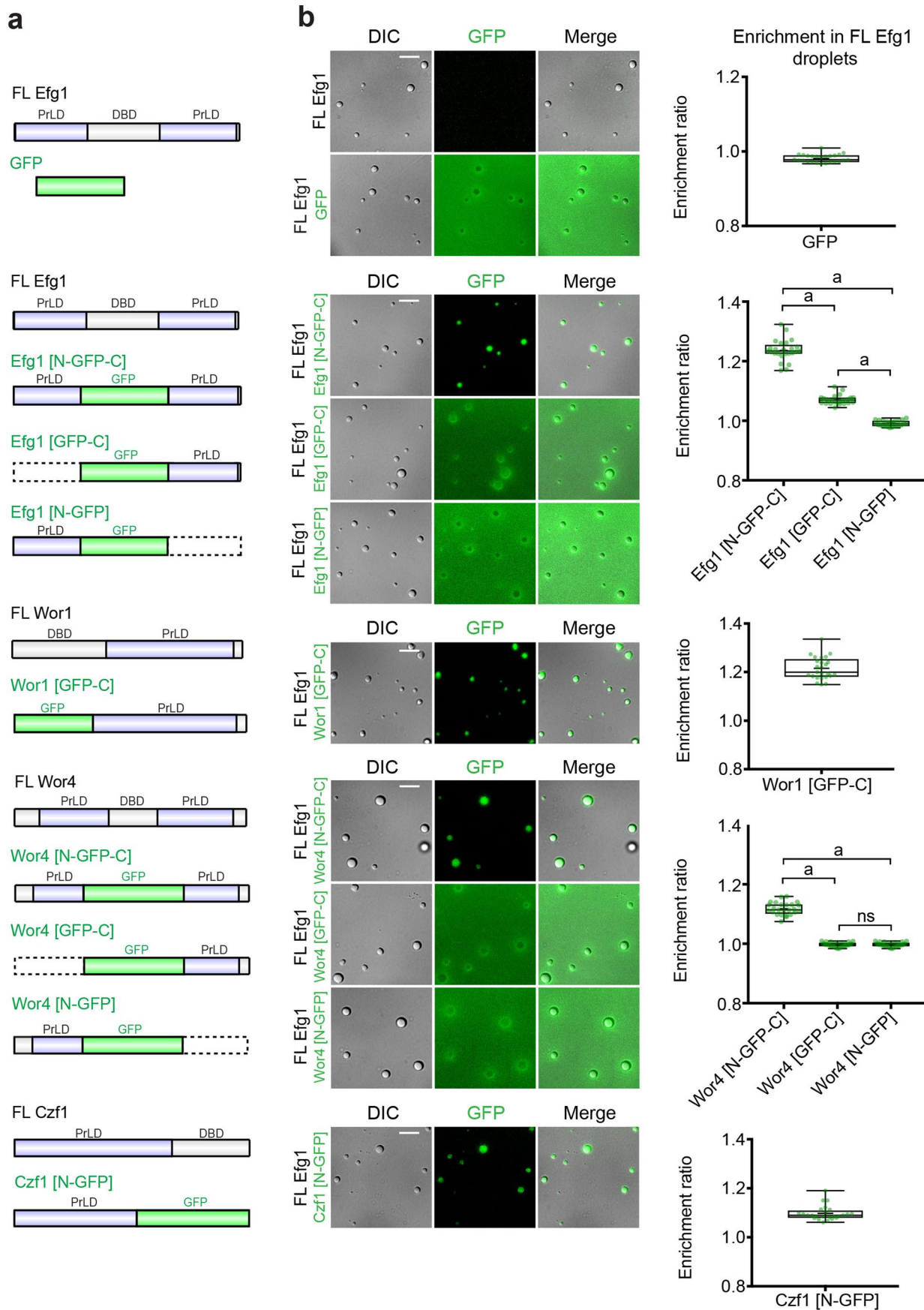
Extended Data Fig. 1 | ChIP-chip data for master white-opaque TFs at select *C. albicans* genes. Top, ChIP-chip enrichment peaks shown for Wor1 (orange), Wor2 (pink), Wor3 (blue), Czf1 (green), Efg1 (purple) and Ahr1 (red). Solid lines indicate TF binding and dotted lines indicate controls. ORFs are represented by purple boxes and lighter purple boxes represent untranslated regions. Bottom, Positions of consensus DNA binding sites for each TF. The large circles represent motif hits with >75% of the maximum score, medium circles represent motif hits that have 50–75% of the maximum score, and small circles represent motif hits that have 25–50% of the maximum score. ChIP enrichment plot generated from data in refs. ^{27,30,36} and motif analysis performed using data from refs. ^{27,30}.



Extended Data Fig. 2 | Purified *C. albicans* white-opaque TFs used in this study. **a**, Schematic of TF expression constructs, including 6x histidine tag, MBP, and TEV protease site. **b**, Purified proteins used in this study. SDS-PAGE gels of *C. albicans* Wor1, Efg1, Czf1 and Wor4 HIS6-MBP-TF fusion proteins, as well as proteins with different PrLD deletions and those where the DBD has been replaced with GFP. **c**, Image of a HIS6-MBP-Efg1 protein solution (30 μ M) without (left) and with (right) the addition of TEV protease for 30 min at 22 °C. Cloudiness indicates formation of phase-separated condensates, as confirmed by microscopy. Protein droplets formed in 10 mM Tris-HCl, pH 7.4, 150 mM NaCl at 22 °C. Scale bar; 5 μ m. Representative data for an experiment repeated more than three times with similar results.

a**b****c****Extended Data Fig. 3 | See next page for caption.**

Extended Data Fig. 3 | Hexanediol treatment selectively disrupts *C. albicans* TF condensates even during co-compartmentalization with other TFs. **a**, Images of Efg1, Czf1, Wor1 (*CaCmWor1*), and Wor4 droplets at the indicated concentrations with or without 10% 1,6- or 2,5-hexanediol. For hexanediol treatment, proteins were incubated with TEV for 30 minutes in 10 mM Tris-HCl, pH 7.4, 150 mM NaCl, at 22 °C, and then mixed with 1,6- or 2,5-hexanediol in the same buffer, incubated for 10 minutes, and imaged. Wor1, Wor4, and Czf1 assays also included 5% PEG-8000. Where indicated for Wor4, hexanediol was added for 10 minutes and then TEV/PEG-8000 added and the sample incubated for an additional 30 minutes prior to imaging. Images represent a single experimental replicate with assays repeated at least twice with similar results. Scale bars; 10 µm. **b**, Representative images of fluorescently labeled Efg1, Wor1 (*CaWor1*), Wor4, and Czf1 proteins compartmentalized within Efg1 condensates, and treated with 10% 1,6- or 2,5-hexanediol. Unlabeled bulk protein (15 µM) was mixed with each of the fluorescently labeled proteins (37.5 nM) in 10 mM Tris-HCl, pH 7.4, 150 mM NaCl. Proteins were then incubated at 22 °C with TEV for 30 minutes and treated with 1,6- or 2,5-hexanediol in the same buffer for 10 minutes prior to imaging. Dylight NHS-Ester labeling of the 4 proteins used fluors of 405, 488, 550 and 633 nm. Images represent a single experimental replicate with assays performed three times with similar results. Scale bar, 10 µm; images are maximum Z-stack projections. **c**, Representative images of fluorescently labeled Efg1, Wor1 (*CaWor1*), Wor4, and Czf1 proteins compartmentalized within Czf1, Wor1(*CaCmWor1*), or Wor4 condensates. Unlabeled bulk proteins (15 µM) were mixed with each of the fluorescently labeled proteins (37.5 nM) in 10 mM Tris-HCl, pH 7.4, 150 mM NaCl. Proteins were then incubated at 22 °C with TEV for 30 min. Dylight NHS-Ester labeling of the 4 proteins used fluors of 488, 550, 405, and 633 nm. Images represent a single experimental replicate, with assays performed three times with similar results. Scale bars, 10 µm; images are maximum Z-stack projections.



Extended Data Fig. 4 | See next page for caption.

Extended Data Fig. 4 | PrLDs enable the co-partitioning of *C. albicans* white-opaque TFs. Analysis of the ability of full-length or truncated TFs to co-partition within Efg1 condensates. **a**, Schematics of the GFP fusion proteins tested in phase separation assays. **b**, Efg1-GFP, Wor4-GFP, Czf1-GFP or Wor1-GFP variants were evaluated for their ability to co-partition with unlabeled Efg1 droplets. For each protein, the DBD was replaced with GFP. In all assays, proteins were incubated with TEV for 30 min at 22 °C in 10 mM Tris-HCl, pH 7.4, 150 mM NaCl. Bulk (full-length) Efg1 was present at 30 μM with 3 μM TF-GFP fusion proteins included in each reaction. Box and whisker plots show all data points, maximum to minimum, and indicate enrichment ratios for each TF-GFP fusion protein with condensates formed by full-length Efg1. For each plot, data are median (line), mean ('+'), 25–75th percentiles (box), and 5–95th percentiles (whiskers). Droplets were located in the DIC channel, and the intensity for the GFP signal inside the droplet compared to the signal intensity outside the droplet, following subtraction of fluorescence background. At least five images were used for quantification, with 25 total droplets measured for each construct. Statistical significance was performed using a two-tailed Mann-Whitney U-test; P-values: a, < 0.0001 ; ns, not significant. Scale bars; 5 μm.

Reporting Summary

Nature Research wishes to improve the reproducibility of the work that we publish. This form provides structure for consistency and transparency in reporting. For further information on Nature Research policies, see our [Editorial Policies](#) and the [Editorial Policy Checklist](#).

Statistics

For all statistical analyses, confirm that the following items are present in the figure legend, table legend, main text, or Methods section.

n/a Confirmed

- The exact sample size (n) for each experimental group/condition, given as a discrete number and unit of measurement
- A statement on whether measurements were taken from distinct samples or whether the same sample was measured repeatedly
- The statistical test(s) used AND whether they are one- or two-sided
Only common tests should be described solely by name; describe more complex techniques in the Methods section.
- A description of all covariates tested
- A description of any assumptions or corrections, such as tests of normality and adjustment for multiple comparisons
- A full description of the statistical parameters including central tendency (e.g. means) or other basic estimates (e.g. regression coefficient) AND variation (e.g. standard deviation) or associated estimates of uncertainty (e.g. confidence intervals)
- For null hypothesis testing, the test statistic (e.g. F , t , r) with confidence intervals, effect sizes, degrees of freedom and P value noted
Give P values as exact values whenever suitable.
- For Bayesian analysis, information on the choice of priors and Markov chain Monte Carlo settings
- For hierarchical and complex designs, identification of the appropriate level for tests and full reporting of outcomes
- Estimates of effect sizes (e.g. Cohen's d , Pearson's r), indicating how they were calculated

Our web collection on [statistics for biologists](#) contains articles on many of the points above.

Software and code

Policy information about [availability of computer code](#)

Data collection	We used AxioVision software (version 4.8) and Zen software (version 3.0 blue edition) from Zeiss to collect fluorescence microscopy images, and CellSens software (version 1.17) from Olympus to collect confocal microscopy images. Single molecule data was collected with Nikon NIS Elements software (version 4.30.02).
Data analysis	We used FIJI/ImageJ (version 1.52p) to visualize images, measure fluorescence intensity and areas, and to determine colocalization of fluorescently tagged proteins. We used GraphPad Prism (version 8.4.2) to perform statistical analysis. Particle tracking analysis was carried out with PAST3 software (version 3.24).

For manuscripts utilizing custom algorithms or software that are central to the research but not yet described in published literature, software must be made available to editors and reviewers. We strongly encourage code deposition in a community repository (e.g. GitHub). See the Nature Research [guidelines for submitting code & software](#) for further information.

Data

Policy information about [availability of data](#)

All manuscripts must include a [data availability statement](#). This statement should provide the following information, where applicable:

- Accession codes, unique identifiers, or web links for publicly available datasets
- A list of figures that have associated raw data
- A description of any restrictions on data availability

Data supporting the findings reported in this study are available upon request from the corresponding author, upon reasonable request. Figures with associated raw data include Figures 3, 4, 5, and 6, and Extended Data Figure 4. The data for these figures is included in Excel file format within this manuscript.

Field-specific reporting

Please select the one below that is the best fit for your research. If you are not sure, read the appropriate sections before making your selection.

Life sciences Behavioural & social sciences Ecological, evolutionary & environmental sciences

For a reference copy of the document with all sections, see nature.com/documents/nr-reporting-summary-flat.pdf

Life sciences study design

All studies must disclose on these points even when the disclosure is negative.

Sample size	At least 10 images were taken per imaging experiment, except for images in Figure 3, where at least 5 images were taken per indicated condition. At least 2 replicates were performed for each experiment, with exact numbers of replicates noted in each figure legend. No sample size calculation was performed for any experiments in this study. Sample sizes were chosen to represent an appropriate level of reproducibility between replicates, and to accurately encompass differences between images/data. We believe the sample sizes are sufficient, as we observed differences between experimental groups with P-values determined to be lower than 0.05.
Data exclusions	No data is excluded from this study.
Replication	Attempts at replication were successful. All experiments were repeated at least two times unless noted differently. Exact numbers of replicates for each experiment are detailed in the figure legends.
Randomization	Randomization was not relevant for this study.
Blinding	Blinding was not relevant for this study.

Reporting for specific materials, systems and methods

We require information from authors about some types of materials, experimental systems and methods used in many studies. Here, indicate whether each material, system or method listed is relevant to your study. If you are not sure if a list item applies to your research, read the appropriate section before selecting a response.

Materials & experimental systems		Methods	
n/a	Involved in the study	n/a	Involved in the study
<input type="checkbox"/>	<input checked="" type="checkbox"/> Antibodies	<input checked="" type="checkbox"/>	<input type="checkbox"/> ChIP-seq
<input type="checkbox"/>	<input checked="" type="checkbox"/> Eukaryotic cell lines	<input checked="" type="checkbox"/>	<input type="checkbox"/> Flow cytometry
<input checked="" type="checkbox"/>	<input type="checkbox"/> Palaeontology and archaeology	<input checked="" type="checkbox"/>	<input type="checkbox"/> MRI-based neuroimaging
<input checked="" type="checkbox"/>	<input type="checkbox"/> Animals and other organisms		
<input checked="" type="checkbox"/>	<input type="checkbox"/> Human research participants		
<input checked="" type="checkbox"/>	<input type="checkbox"/> Clinical data		
<input checked="" type="checkbox"/>	<input type="checkbox"/> Dual use research of concern		

Antibodies

Antibodies used	All antibodies used are commercially available antibodies. Nucleosomes were labeled using a rabbit α -HA antibody (ICL, RHGT-45A-Z) against the 3xHA epitope on histone H2A followed by binding of an Alexa-488 conjugated α -Rabbit antibody (Thermo Fisher, A-11008). Digylated DNA ends were detected with anti-Dig antibodies (Life Tech, 9H27L19) followed with goat anti-rabbit antibody-conjugated quantum dots (Life Tech, Q-11461MP).
Validation	Rabbit α -HA antibody (ICL, RHGT-45A-Z) was validated by the manufacturer, Immunology Consultants Laboratory, Inc. ICL notes that, "Rabbits were immunized with highly purified YPYDVPDYA (influenza hemagglutinin-HA-epitope) and the resulting antiserum was collected. Antibody was immunoaffinity purified off an antigen containing immunosorbent. Antibody concentration was determined using an absorbance at 280 nm: 1.4 equals 1.0mg of IgG." Further information relating to this antibody, including relevant publications, can be found at the ICL website (http://www.icllab.com/anti-ha-tag-antibody-rabbit.html). Alexa-488 conjugated α -Rabbit antibody (Thermo Fisher, A-11008) was validated by the manufacturer, ThermoFisher Scientific. This antibody has been cited in over 400 publications, and further information is available on the ThermoFisher website (https://www.thermofisher.com/antibody/product/Goat-anti-Rabbit-IgG-H-L-Cross-Adsorbed-Secondary-Antibody-Polyclonal/A-11008). The anti-Dig antibody was tested by the manufacturer against recombinant digoxigenin conjugated to BSA, and the antibody-conjugated quantum dots were purified F(ab')2-goat anti-rabbit IgG antibodies conjugated to Qdot 705.

Eukaryotic cell lines

Policy information about [cell lines](#)

Cell line source(s)

The U2OS LacI reporter cell line was a gift from the Tjian lab (Robert Tjian, UC Berkeley)

Authentication

Use of this cell line is analogous to that in Chong et al., Science, 2018, Jul 27;361(6400). doi: 10.1126/science.aar2555. We received this cell line directly from the Tjian lab, and as such it was not independently authenticated in our lab.

Mycoplasma contamination

Cells tested negative for mycoplasma contamination in the Tjian lab.

Commonly misidentified lines
(See [ICLAC](#) register)

No ICLAC lines were used in this study.